

Coupled Hierarchical Structure Learning using Tree-Wasserstein Distance

Ya-Wei Eileen Lin¹, Ronald R. Coifman², Gal Mishne³, and Ronen Talmon¹

¹Technion - Israel Institute of Technology ²Yale University ³University of California San Diego

Abstract

In many applications, both data samples and features have underlying hierarchical structures. However, existing methods for learning these latent structures typically focus on either samples or features, ignoring possible coupling between them. In this paper, we introduce a coupled hierarchical structure learning method using tree-Wasserstein distance (TWD). Our method jointly computes TWDs for samples and features, representing their latent hierarchies as trees. We propose an iterative, unsupervised procedure to build these sample and feature trees based on diffusion geometry, hyperbolic geometry, and wavelet filters. We show that this iterative procedure converges and empirically improves the quality of the constructed trees. The method is also computationally efficient and scales well in high-dimensional settings. Our method can be seamlessly integrated with hyperbolic graph convolutional networks (HGCN). We demonstrate that our method outperforms competing approaches in sparse approximation and unsupervised Wasserstein distance learning on several word-document and single-cell RNA-sequencing datasets. In addition, integrating our method into HGCN enhances performance in link prediction and node classification tasks.

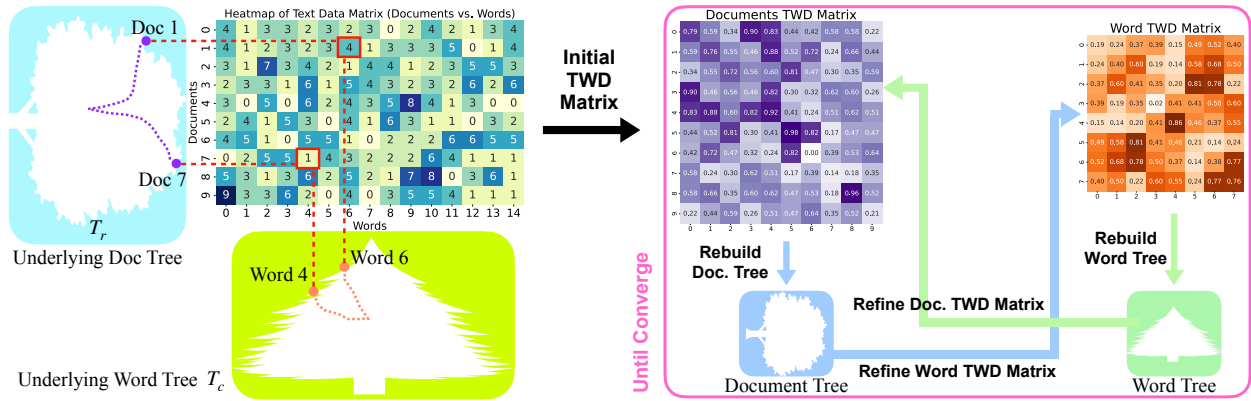


Figure 1: Overview of coupled hierarchical structure learning (CoHSL) using tree-Wasserstein distance (TWD) for a data matrix. The hidden hierarchical structures exist in both rows (i.e., samples) and columns (i.e., features), and they are codependent and often hidden. CoHSL using TWD jointly uncovers intrinsic distances between samples and between features in an unsupervised manner such that the hierarchical structure within each mode informs and shapes the other during the learning process.

1 Introduction

Data with hierarchical structures is prevalent across various domains. Existing methods for hierarchy learning typically focus on the hierarchy underlying either samples or features [Wang and Wang, 2013, Hong et al., 2018, Weber et al., 2024], but not both. For instance, hyperbolic geometry [Ratcliffe et al., 1994] has been accentuated in hierarchical graph representation learning [Nickel and Kiela, 2017, Chami et al., 2019], where methods typically learn hyperbolic embeddings for nodes (i.e., samples) based on a (partially) known graph. However, many types of data, e.g., gene expression data [Tanay and Regev, 2017, Bellazzi et al., 2021, Luecken and Theis, 2019], images [Dabov et al.,

2007, Ulyanov et al., 2018, Mettes et al., 2024], word-document datasets [Chang and Blei, 2010, Kusner et al., 2015, Huang et al., 2016], citation networks [Sen et al., 2008, Leicht and Newman, 2008, Clauset et al., 2008], and sensor networks [Iwanicki and van Steen, 2009, Mir and Ko, 2007], exhibit hidden, codependent hierarchical structures that underlie both samples and features. Thus, finding meaningful distance metrics between samples and between features, which account for these intrinsic, coupled hierarchical structures, is a crucial task. Unlike traditional approaches, which typically focus on either sample or feature hierarchy, we aim to jointly learn these hierarchies leveraging their codependence.

To this end, in this paper, we propose a method that consists of three main components. First, given a data matrix with samples in the rows and features in the columns, we construct one tree to represent the samples (rows) and another to represent the features (columns). Next, to combine the trees of the two modes (rows and columns), we apply the tree-Wasserstein distance (TWD) [Indyk and Thaper, 2003] to incorporate the inferred tree of one mode (e.g., rows) to compute distances in the other mode (e.g., columns). Specifically, we use the feature tree to compute the sample TWD and the sample tree to compute the feature TWD. The trees inference and TWD computation are based on the method in Lin et al. [2024a], making use of diffusion geometry [Coifman and Lafon, 2006] and hyperbolic geometry [Bowditch, 2007], which has proven effective in recovering latent hierarchies through tree construction. Third, we iteratively alternate the tree inference and TWD computation between the two modes to refine the trees and distances of the samples and features. Specifically, each iteration uses the sample TWD to refine the inference of the sample tree, which, in turn, defines a new feature TWD. Similarly, the feature TWD is used to refine the inference of the feature tree, which, in turn, defines a new sample TWD (see Fig. 1). We term this approach as *coupled hierarchical structure learning (CoHSL)*, designed for data matrix with underlying hierarchical structures in both samples and features.

Contribution. Our main contributions are as follows.

- We study the problem of coupled hierarchical structure learning for data with latent hierarchies in both samples and features. This is a common structure in various applications, yet it is often overlooked in existing work that typically addresses only a single mode.
- We introduce CoHSL, an iterative approach for coupled hierarchical learning that captures the intrinsic hierarchical structures underlying both the samples and the features through TWD. In addition, we introduce an improved method that incorporates Haar wavelets [Haar, 1911] with the CoHSL iterative process. Haar wavelets are derived from a dyadic tree, so using them to filter data strengthens its hierarchy and enhances the effectiveness of CoHSL.
- We theoretically show that the proposed iterative methods converge and guarantee the existence of solutions in the form of coupled TWDs.
- We showcase the effectiveness of integrating our methods into hyperbolic graph convolution neural networks [Chami et al., 2019, Dai et al., 2021] to improve the link prediction and node classification tasks. In addition, we demonstrate empirical advantages in sparse approximation and unsupervised Wasserstein distance learning tasks for word-document data and single-cell RNA-sequencing data.

2 Related Work

We provide a brief overview of related work here and refer to App. A and B for a more in-depth discussion.

Tree-Wasserstein Distance. TWD [Indyk and Thaper, 2003, Evans and Matsen, 2012, Yamada et al., 2022] has been proposed to reduce the computational complexity of the Wasserstein distance [Villani, 2009], which is a powerful tool to compare distributions. TWD methods typically involve two steps: constructing a feature tree and using this tree to calculate a sample TWD. In most cases, the constructed tree approximates the *Euclidean* ground metric, without capturing *latent* hierarchical relationships. Recently, [Lin et al., 2024a] proposed integrating TWD with hyperbolic embeddings, enabling the tree metric to reflect geodesic distances on a latent unobserved tree. However, these methods do not consider *coupled* hierarchical structures of samples and features.

Bi-Clustering. Bi-clustering [Govaert and Nadif, 2008] is designed to simultaneously identify clusters for both rows and columns. The convex biclustering approach [Chi et al., 2017] relies on convex clustering, which provides a hierarchy of nested clusters [Chi and Lange, 2015, Chi and Steinerberger, 2019]. Yet, the typical imposed bi-clustering structure can be overly rigid [Madeira and Oliveira, 2004], potentially distorting the intrinsic geometry and failing to reflect underlying relationships [Mishne et al., 2019]. This is especially evident when the data involves overlapping rather than disjoint clusters, as in word-document matrices [Ahn et al., 2010].

Co-Manifold Learning. The codependency between feature relationships informed by sample relationships, and vice versa, has been studied in Ankenman [2014], Gavish and Coifman [2012], Gavish et al. [2010], Yair et al. [2017], Leeb and Coifman [2016] for co-organization of data matrices, and in Mishne et al. [2016], Shahid et al. [2016], Mishne et al. [2019] for dimensionality reduction across both samples and features. While these approaches assume a manifold structure, we consider an underlying hierarchical structure instead.

3 Background

Notation. For $n \in \mathbb{N}$, we denote $[n] = \{1, \dots, n\}$. Let $\mathbf{X} \in \mathbb{R}_+^{n \times m}$ represent a data matrix with n rows (samples) and m columns (features). Let $\mathbf{X}_{i,:}$ and $\mathbf{X}_{:,j}$ denotes the i -th row and j -th column of \mathbf{X} , respectively. The discrete histogram with m bins is denoted by $\Delta_m = \{\mathbf{h} \in \mathbb{R}_+^m \mid \|\mathbf{h}\|_1 = 1\}$. An undirected weighted graph is denoted by $G = (V, E, \mathbf{A})$ with vertex set V , the edge set E , and the symmetric weights matrix $\mathbf{A} \in \mathbb{R}_+^{|V| \times |V|}$. Let $\langle \cdot, \cdot \rangle$ be the standard inner product and $\|\cdot\|_1$ is the matrix l_1 norm.

Hyperbolic Geometry. Hyperbolic geometry is a non-Euclidean Riemannian geometry with constant negative curvature. We consider two equivalent models of hyperbolic space [Ratcliffe et al., 1994]: the Poincaré half-space and the hyperboloid model. The Poincaré half-space was used for embedding that reveals the hierarchical structure underlying data, while the hyperboloid model is advantageous for its simple closed-form Riemannian operations [Nickel and Kiela, 2018].

The d -dimensional Poincaré half-space is defined as $\mathbb{H}^d = \{\mathbf{a} \in \mathbb{R}^d \mid \mathbf{a}(d) > 0\}$ with the Riemannian metric tensor $ds^2 = (d\mathbf{a}^2(1) + \dots + d\mathbf{a}^2(d))/\mathbf{a}^2(d)$ [Beardon, 2012]. Let \mathbb{L}^d denote the hyperboloid manifold in d dimensions, defined by $\mathbb{L}^d = \{\mathbf{b} \in \mathbb{R}^{d+1} \mid \langle \mathbf{b}, \mathbf{b} \rangle_{\mathcal{L}} = -1, \mathbf{b}(1) > 0\}$, where $\langle \cdot, \cdot \rangle_{\mathcal{L}}$ is the Minkowski inner product $\langle \mathbf{b}, \mathbf{b} \rangle_{\mathcal{L}} = \mathbf{b}^\top [-1, \mathbf{0}^\top; \mathbf{0}, \mathbf{I}_d] \mathbf{b}$.

Tree-Wasserstein Distance. Consider a tree $T = (V, E, \mathbf{A})$. The tree distance $d_T : V \times V \rightarrow \mathbb{R}_+$ is the sum of weights of the edges on the shortest path between any two nodes on the tree T . Let $\Upsilon_T(v)$ be the set of nodes in the subtree of T rooted at $v \in V$. For any $u \in V$, there exists a unique parent node v s.t. $w_u = d_T(u, v)$ [Cormen et al., 2022, Bondy and Murty, 2008]. Given two discrete histograms $\rho_1, \rho_2 \in \Delta_{|V|}$ supported on T , the tree-Wasserstein distance (TWD) [Indyk and Thaper, 2003] is defined by

$$\text{TW}(\rho_1, \rho_2, T) = \sum_{v \in V} w_v \left| \sum_{u \in \Upsilon_T(v)} (\rho_1(u) - \rho_2(u)) \right|. \quad (1)$$

4 Coupled Hierarchical Structure Learning

We consider a data matrix $\mathbf{X} \in \mathbb{R}_+^{n \times m}$, where n denotes the number of samples (rows) and m denotes the number of features (columns). Suppose both rows and columns exhibit codependent latent hierarchical structures. The hidden hierarchies are modeled by a rooted weighted tree $T_r = ([n], E_r, \mathbf{A}_r, \mathbf{X})$ for the samples and $T_c = ([m], E_c, \mathbf{A}_c, \mathbf{X}^\top)$ for the features. Here, E_r (resp. E_c) denotes the edge set for samples (resp. features), $\mathbf{A}_r \in \mathbb{R}_+^{n \times n}$ (resp. $\mathbf{A}_c \in \mathbb{R}_+^{m \times m}$) is the sample (resp. feature) weight matrix, and the data matrix \mathbf{X} (resp. \mathbf{X}^\top) contains n sample attributes in m dimensions (resp. m feature attributes in n dimensions). We assume that the data matrix \mathbf{X} reflects the underlying hierarchical structures, with smooth variation across samples and features relative to the graph connectivity of the

respective tree. To this end, we define the coupled hierarchical structure learning problem as

$$\min_{\mathbf{W}_r, \mathbf{W}_c} \mathcal{L}(\mathbf{W}_r, \mathbf{W}_c) = \lambda_r \sum_{i, i'} (\mathbf{W}_r(i, i') - \text{TW}(\mathbf{r}_i, \mathbf{r}_{i'}, T_c))^2 + \lambda_c \sum_{j, j'} (\mathbf{W}_c(j, j') - \text{TW}(\mathbf{c}_j, \mathbf{c}_{j'}, T_r))^2 \quad (2)$$

for some $\lambda_c, \lambda_r > 0$ balancing between rows and columns based on their cardinality, where $\Delta_m \ni \mathbf{r}_i = \mathbf{X}_{i,:}^\top / \|\mathbf{X}_{i,:}\|_1$, and $\Delta_n \ni \mathbf{c}_j = \mathbf{X}_{:,j} / \|\mathbf{X}_{:,j}\|_1$. Note that Eq. (2) relates to metric multidimensional scaling [Cox and Cox, 2000, Sala et al., 2018], which matches distances with a specified dissimilarity matrix to approximate target distances. Here, our approach extends this by addressing both data modes and coupling them, where \mathbf{W}_r and \mathbf{W}_c approximate TWD on T_c and T_r for samples and features, respectively. By jointly optimizing them, we aim to find a pair of meaningful distances that respect the latent coupled hierarchical structures.

4.1 Learning Latent Coupled Trees

The challenge of solving Eq. (2) is two-fold. First, the trees T_r and T_c are codependent and often not explicitly known, and we are only provided with the observational \mathbf{X} . Second, solving the optimization problem in Eq. (2) exactly may be computationally intractable, necessitating approximate, more efficient solutions. To cope with these two challenges, we propose an iterative approach by alternately optimizing \mathbf{W}_c or \mathbf{W}_r while keeping the other fixed. We will theoretically show the convergence of this approach and demonstrate empirically that it yields a useful solution.

Overview. Our *Coupled Hierarchical Structure Learning (CoHSL)* approach consists of three main steps.

- (a) **Initialize trees:** We construct an initial sample tree $\hat{T}_r^{(0)}(\mathbf{M}_r)$ and an initial feature tree $\hat{T}_c^{(0)}(\mathbf{M}_c)$ based on the initial pairwise sample distances $\mathbf{M}_r \in \mathbb{R}^{n \times n}$ and feature distances $\mathbf{M}_c \in \mathbb{R}^{m \times m}$.
- (b) **Initial TWDs:** We use the initial feature tree to compute an initial sample TWD matrix, $\mathbf{W}_r^{(0)}(i, i') = \text{TW}(\mathbf{r}_i, \mathbf{r}_{i'}, \hat{T}_c^{(0)}(\mathbf{M}_c)) \forall i, i' \in [n]$, and use the initial sample tree to compute an initial feature TWD matrix, $\mathbf{W}_c^{(0)}(j, j') = \text{TW}(\mathbf{c}_j, \mathbf{c}_{j'}, \hat{T}_r^{(0)}(\mathbf{M}_r)) \forall j, j' \in [m]$.
- (c) **Iterate:** We employ an iterative procedure that alternately updates the trees and TWD matrices. Specifically, for $l \geq 0$, based on the sample TWD matrix $\mathbf{W}_r^{(l)}$, we rebuild the sample tree $\hat{T}_r^{(l+1)}(\mathbf{W}_r^{(l)})$, and based on the feature TWD matrix $\mathbf{W}_c^{(l)}$, we rebuild the feature tree $\hat{T}_c^{(l+1)}(\mathbf{W}_c^{(l)})$. Then, these refined trees, $\hat{T}_r^{(l+1)}(\mathbf{W}_r^{(l)})$ and $\hat{T}_c^{(l+1)}(\mathbf{W}_c^{(l)})$, are used to update the TWD matrices: $\mathbf{W}_r^{(l+1)}(i, i') = \text{TW}(\mathbf{r}_i, \mathbf{r}_{i'}, \hat{T}_c^{(l+1)}(\mathbf{W}_c^{(l)}))$ and $\mathbf{W}_c^{(l+1)}(j, j') = \text{TW}(\mathbf{c}_j, \mathbf{c}_{j'}, \hat{T}_r^{(l+1)}(\mathbf{W}_r^{(l)}))$. We repeat these updates until convergence. Our goal is to reach an equilibrium where the TWDs respect the latent T_r and T_c .

Single-Mode Tree-Wasserstein Distance. Unlike typical TWD methods [Indyk and Thaper, 2003, Evans and Matsen, 2012, Sato et al., 2020, Le et al., 2019, Yamada et al., 2022], which use trees to efficiently compute the Wasserstein distance with *Euclidean* ground metric, here we use the hyperbolic diffusion tree [Lin et al., 2024a], to reveal the latent hierarchical structure. The hyperbolic diffusion tree allows us to compute TWDs that respect the underlying hierarchical structure within high-dimensional data. We first compute the sample TWD matrix as follows. Given an *initial* feature pairwise distance matrix $\mathbf{M}_c \in \mathbb{R}^{m \times m}$, the feature hyperbolic diffusion tree $\hat{T}_c^{(0)}(\mathbf{M}_c)$ is a complete binary tree with m leaves (see App. A for details). The sample TWD between two samples based on the feature hyperbolic diffusion tree is

$$\mathbf{W}_r^{(0)}(i, i') = \text{TW}(\mathbf{r}_i, \mathbf{r}_{i'}, \hat{T}_c^{(0)}(\mathbf{M}_c)) + \gamma_r \zeta(\mathbf{r}_i, \mathbf{r}_{i'}), \quad (3)$$

where $\gamma_r \geq 0$ and ζ is the regularization function $\zeta(\mathbf{r}_i, \mathbf{r}_{i'}) = \frac{1}{2} \int_0^{\|\mathbf{r}_i - \mathbf{r}_{i'}\|_2} \frac{1}{\sqrt{\xi + 10^{-6}}} d\xi$. We employ a regularization function $\zeta(\cdot, \cdot)$, which monotonically increases on $[0, \infty)$ and penalizes small differences more significantly than larger differences for smoothness [Mishne et al., 2019]. For brevity, we represent the matrix $\mathbf{W}_r^{(0)} \in \mathbb{R}^{n \times n}$ as the output of an operator acting on \mathbf{R} to generate the sample TWD matrix

$$\mathbf{W}_r^{(0)} = \Phi_{\mathbf{R}}(\mathbf{M}_c), \quad (4)$$

Algorithm 1 CoHSL using TWD

Input: Data matrix $\mathbf{X} \in \mathbb{R}_+^{n \times m}$, initial distance matrices $\mathbf{M}_c \in \mathbb{R}^{m \times m}$ and $\mathbf{M}_r \in \mathbb{R}^{n \times n}$, γ_r and γ_c

Output: Coupled TWD matrices $\mathbf{W}_r^{(l)}$ and $\mathbf{W}_c^{(l)}$

for $i \in [n]$ **do**

$\mathbf{r}_i \leftarrow \mathbf{X}_{i,:}^\top / \|\mathbf{X}_{i,:}\|_1$

for $j \in [m]$ **do**

$\mathbf{c}_j \leftarrow \mathbf{X}_{:,j} / \|\mathbf{X}_{:,j}\|_1$

$l \leftarrow 0$, $\mathbf{R} \leftarrow [\mathbf{r}_1, \dots, \mathbf{r}_n]$ and $\mathbf{C} \leftarrow [\mathbf{c}_1, \dots, \mathbf{c}_m]$

$\mathbf{W}_r^{(0)} \leftarrow \Phi_{\mathbf{R}}(\mathbf{M}_c)$ and $\mathbf{W}_c^{(0)} \leftarrow \Phi_{\mathbf{C}}(\mathbf{M}_r)$

repeat

$\mathbf{W}_r^{(l+1)} \leftarrow \Phi_{\mathbf{R}}(\mathbf{W}_c^{(l)})$ and $\mathbf{W}_c^{(l+1)} \leftarrow \Phi_{\mathbf{C}}(\mathbf{W}_r^{(l)})$

$l \leftarrow l + 1$

until convergence

where $\mathbf{R} = [\mathbf{r}_1, \dots, \mathbf{r}_n]$. Similarly, given an *initial* sample pairwise distance $\mathbf{M}_r \in \mathbb{R}^{n \times n}$, the sample hyperbolic diffusion tree $\widehat{T}_r^{(0)}(\mathbf{M}_r)$ is built and used to compute the feature TWD matrix, which is defined in the same manner $\mathbb{R}^{m \times m} \ni \mathbf{W}_c^{(0)} = \Phi_{\mathbf{C}}(\mathbf{M}_r)$, where $\mathbf{C} = [\mathbf{c}_1, \dots, \mathbf{c}_m]$.

Alternately Updating the Coupled Trees and TWDs. To solve Eq. (2), we propose an iterative method that considers the interplay between T_r and T_c . Specifically, the coupled TWD matrices are updated alternately

$$\mathbf{W}_r^{(l+1)} = \Phi_{\mathbf{R}}(\mathbf{W}_c^{(l)}) \text{ and } \mathbf{W}_c^{(l+1)} = \Phi_{\mathbf{C}}(\mathbf{W}_r^{(l)}), \quad (5)$$

for $l \geq 0$. Through the iterative refinement of $\mathbf{W}_c^{(l)}$ and $\mathbf{W}_r^{(l)}$, we aim to capture an intrinsic and stable representation of the coupled hierarchical structures, and reach a stationary point, where the equilibrium conditions hold

$$\mathbf{W}_r^{(l)} = \Phi_{\mathbf{R}}(\mathbf{W}_c^{(l)}), \text{ and } \mathbf{W}_c^{(l)} = \Phi_{\mathbf{C}}(\mathbf{W}_r^{(l)}). \quad (6)$$

We outline the proposed CoHSL in Alg. 1. Note that the alternating updates in Eq. (5) correspond to a coordinate descent method [Wright, 2015, Friedman et al., 2010] for minimizing the objective function in Eq. (2) with a regularization, where each update optimizes \mathcal{L} w.r.t. one variable while holding the other fixed. By iteratively applying these updates, each step reduces the value of \mathcal{L} as $\mathcal{L}(\mathbf{W}_r^{(l+1)}, \mathbf{W}_c^{(l)}) \leq \mathcal{L}(\mathbf{W}_r^{(l)}, \mathbf{W}_c^{(l)})$ and $\mathcal{L}(\mathbf{W}_r^{(l)}, \mathbf{W}_c^{(l+1)}) \leq \mathcal{L}(\mathbf{W}_r^{(l)}, \mathbf{W}_c^{(l)})$. In addition, since \mathcal{L} is convex in each variable, this process converges to a stationary point of \mathcal{L} . Hence, the alternating solution is equivalent to solving the optimization problem with regularization, achieving a local minimum w.r.t. both [Horst and Tuy, 2013].

Theorem 1. *The sequences $\mathbf{W}_r^{(l)}$ and $\mathbf{W}_c^{(l)}$ for $l \geq 1$ generated by CoHSL have at least one limit point, and all limit points are stationary points of Eq. (6) if $\gamma_r, \gamma_c > 0$.*

The proof of Thm. 1 is in App. C. In addition, the mappings $\Phi_{\mathbf{R}}(\mathbf{W}_c^{(l)})$ and $\Phi_{\mathbf{C}}(\mathbf{W}_r^{(l)})$ are Lipschitz continuous, positively 1-homogeneous and monotone [Huizing et al., 2022]. Note that CoHSL can be implemented in practice without regularization. However, the conditions $\gamma_r, \gamma_c > 0$ are necessary for the theoretical guarantees provided by Thm. 1. The regularization supports the convergence but leads to an approximate, rather than exact, solution. While alternative forms of regularization, e.g., entropic regularization [Cuturi, 2013], could be considered, we show that it is less effective in App. E.

4.2 Learning Coupled Trees with Wavelet Filters

Given the complete binary tree $\widehat{T}_c^{(1)}(\widehat{\mathbf{W}}_c^{(0)})$ with m leaves, where $\widehat{\mathbf{W}}_c^{(0)} = \Phi_{\mathbf{C}}(\mathbf{M}_r)$ is the initial feature TWD matrix, we can build Haar wavelets as follows. Let $\ell = 1, \dots, L_c$ denote the levels in the tree, where $\ell = 1$ is the root level and $\ell = L_c$ is the leaf level. Let $\widehat{\Upsilon}_c(\ell, s)$ be the set of all leaves in the subtree, whose root is the s -th node of the tree at level ℓ , where $s = 1, \dots, N_\ell$ and N_ℓ is the number of nodes in the ℓ -level. At level ℓ , a subtree $\widehat{\Upsilon}_c(\ell, s)$ splits into

two sub-subtrees $\widehat{Y}_c(\ell + 1, s_1)$ and $\widehat{Y}_c(\ell + 1, s_2)$. A zero-mean Haar wavelet $\psi_{\ell,s} \in \mathbb{R}^m$ has non-zero values only at the indices corresponding to leaves in the sub-subtrees and is piecewise constant on each of them (see App. A for an illustration). The set of these Haar wavelets, along with a constant vector, is complete and forms an orthonormal Haar basis, denoted by $\Psi \in \mathbb{R}^{m \times m}$ with each column corresponding to a Haar wavelet (basis vector). Any sample $\mathbf{X}_{i,:} \in \mathbb{R}^m$ can be expanded in this Haar basis as $\mathbf{X}_{i,:} = \sum_{\ell,\varepsilon} \alpha_{i,\ell,\varepsilon} \psi_{\ell,\varepsilon}$, where $\alpha_{i,\ell,s} = \langle \mathbf{X}_{i,:}, \psi_{\ell,s} \rangle$ is the expansion coefficient. Let $\boldsymbol{\alpha}_i \in \mathbb{R}^m$ denote the vector of all m expansion coefficients of the i -th sample $\mathbf{X}_{i,:}$.

To construct the Haar wavelet filter [Mallat, 1999, Gavish et al., 2010], we select a subset of d Haar basis vectors denoted by Ω . This filter is represented by the matrix $\Psi_\Omega \in \mathbb{R}^{m \times d}$. The selection of Ω is based on the L_1 norm of expansion coefficients across all samples in the Haar basis. Specifically, we define $\eta = \sum_{i=1}^n \|\boldsymbol{\alpha}_i\|_1$ as sum of the L_1 norm for all samples, while $\eta_\Omega = \sum_{i=1}^n \sum_{q \in \Omega} |\alpha_i(q)|$ represents the L_1 norm for samples in the subset Ω . To identify the most relevant features, we calculate the score $\sum_{i=1}^n |\alpha_i(j)|$ for each feature $j \in [m]$ and arrange the features in descending order based on this score. The subset Ω is built by sequentially adding Haar basis vectors according to this order until the ratio $\frac{\eta_\Omega}{\eta}$ exceeds a threshold $\vartheta_c > 0$. The wavelet filter Ψ_Ω is applied to the data matrix by

$$\varphi_{\widehat{\mathbf{W}}_c^{(0)}}(\mathbf{X}) = (\mathbf{X}\Psi_\Omega)\Psi_\Omega^\top. \quad (7)$$

In an analogous way, the wavelet filter applied to the features, $\varphi_{\widehat{\mathbf{W}}_r^{(0)}}(\mathbf{Z})$, is defined with some constant $\vartheta_r > 0$, where $\mathbf{Z} = \mathbf{X}^\top$, $\widehat{\mathbf{W}}_r^{(0)} = \Phi_{\mathbf{R}}(\mathbf{M}_c)$, and the Haar wavelets are induced by the sample tree $\widehat{T}_r^{(1)}(\widehat{\mathbf{W}}_r^{(0)})$ with n leaves.

The Haar wavelets [Haar, 1911, Mallat, 1989, Daubechies, 1990] are derived from a dyadic tree that aligns with hierarchical data. Therefore, filtering the data through the Haar wavelets reveals the data’s multi-level structure, supporting a clearer representation of the underlying hierarchical relationships [Do and Vetterli, 2005]. When integrated into the iterative procedure in CoHSL, this filtering makes the learning of the underlying coupled hierarchical structures more effective. Specifically, at each iteration, after the inference of the trees and the computation of the corresponding TWD matrices, we filter the samples and features by $\mathbf{X}^{(l+1)} = \varphi_{\widehat{\mathbf{W}}_c^{(l)}}(\mathbf{X}^{(l)})$ and $\mathbf{Z}^{(l+1)} = \varphi_{\widehat{\mathbf{W}}_r^{(l)}}(\mathbf{Z}^{(l)})$ for $l \geq 0$. In the next iteration, we use the filtered data, which is normalized into discrete histograms for TWD computation. This iterative process gives rise to a sequence of TWD matrices $\widehat{\mathbf{W}}_c^{(l)}$ and $\widehat{\mathbf{W}}_r^{(l)}$, where trees are learned from the filtered data with enhanced hierarchical structures by Haar wavelet filtering. Consequently, the data used to construct the trees, and thus the TWDs, evolves with each iteration. The goal of this process is to reach a stationary point:

$$\widehat{\mathbf{W}}_r^{(l)} = \Phi_{\mathbf{R}^{(l)}}(\widehat{\mathbf{W}}_c^{(l)}) \text{ and } \widehat{\mathbf{W}}_c^{(l)} = \Phi_{\mathbf{C}^{(l)}}(\widehat{\mathbf{W}}_r^{(l)}). \quad (8)$$

We present this implementation of CoHSL using Haar wavelet filters in Alg. 2 and term it *CoHSL-Wavelet*.

Theorem 2. *The sequences $\widehat{\mathbf{W}}_r^{(l)}$ and $\widehat{\mathbf{W}}_c^{(l)}$ for $l \geq 1$ generated by CoHSL-Wavelet have at least one limit point, and all limit points are stationary points of Eq. (8) if $\gamma_r, \gamma_c > 0$.*

The proof of Thm. 2 is in App. C. We present an enhanced algorithm that incorporates wavelets into CoHSL, which achieves convergence and refines the coupled hierarchical learning, making it more effective in capturing latent coupled hierarchical structures, as demonstrated in Sec. 6.

We conclude this section with a few remarks. First, the proposed iterative procedure is generalizable and applicable to any TWD method. However, the theoretical results and hidden hierarchy recovery both stem from the hyperbolic diffusion tree [Lin et al., 2024a] and might not hold otherwise. Second, for sufficiently large γ_r and γ_c , the obtained TWDs are unique. This means that even if the initial distances are random, our methods will converge to unique TWDs, as shown in App. E. Third, computing pairwise distance matrices and applying tree decoding with eigendecomposition seemingly restrict applicability to small datasets. However, using the method in Shen and Wu [2022], the TWDs are computed in $O(n^{1.2} + m^{1.2})$ compared to the naïve implementation that requires $O(mn^3 + m^3 \log m + nm^3 + n^3 \log n)$ in each iteration (see App. D). As a result, as shown in Sec. 6, our methods can handle datasets with thousands of samples and features. Finally, the assumption of latent hierarchical structures underlying both samples and features can be relaxed. Either T_r or T_c can be provided as a prior and used for initialization in our methods, as illustrated in Sec. 5.

Algorithm 2 CoHSL-Wavelet

Input: Matrix $\mathbf{X} \in \mathbb{R}_+^{n \times m}$, initial $\mathbf{M}_c \in \mathbb{R}^{m \times m}$ and $\mathbf{M}_r \in \mathbb{R}^{n \times n}$, regularizations γ_r and γ_c , ratios ϑ_c and ϑ_r

Output: Coupled TWD matrices $\widehat{\mathbf{W}}_r$ and $\widehat{\mathbf{W}}_c$

$l \leftarrow 0$ and $\mathbf{Z} \leftarrow \mathbf{X}^\top$

$\widehat{\mathbf{W}}_r^{(0)} \leftarrow \Phi_{\mathbf{R}}(\mathbf{M}_c)$ and $\widehat{\mathbf{W}}_c^{(0)} \leftarrow \Phi_{\mathbf{C}}(\mathbf{M}_r)$

$\mathbf{X}^{(0)} \leftarrow \varphi_{\widehat{\mathbf{W}}_c^{(0)}}(\mathbf{X})$ and $\mathbf{Z}^{(0)} \leftarrow \varphi_{\widehat{\mathbf{W}}_r^{(0)}}(\mathbf{Z})$

repeat

for $i \in [n]$ **do**

$\mathbf{r}_i^{(l)} \leftarrow (\mathbf{X}_{i,:}^{(l)})^\top / \|\mathbf{X}_{i,:}^{(l)}\|_1$

for $j \in [m]$ **do**

$\mathbf{c}_j^{(l)} \leftarrow (\mathbf{Z}_{j,:}^{(l)})^\top / \|\mathbf{Z}_{j,:}^{(l)}\|_1$

$\mathbf{R}^{(l)} \leftarrow [\mathbf{r}_1^{(l)}, \dots, \mathbf{r}_n^{(l)}]$ and $\mathbf{C}^{(l)} \leftarrow [\mathbf{c}_1^{(l)}, \dots, \mathbf{c}_m^{(l)}]$

$\widehat{\mathbf{W}}_r^{(l+1)} \leftarrow \Phi_{\mathbf{R}^{(l)}}(\widehat{\mathbf{W}}_c^{(l)})$ and $\widehat{\mathbf{W}}_c^{(l+1)} \leftarrow \Phi_{\mathbf{C}^{(l)}}(\widehat{\mathbf{W}}_r^{(l)})$

$\mathbf{X}^{(l+1)} \leftarrow \varphi_{\widehat{\mathbf{W}}_c^{(l)}}(\mathbf{X}^{(l)})$ and $\mathbf{Z}^{(l+1)} \leftarrow \varphi_{\widehat{\mathbf{W}}_r^{(l)}}(\mathbf{Z}^{(l)})$

$l \leftarrow l + 1$

until convergence

5 Incorporating CoHSL with HGCN

We illustrate that CoHSL and CoHSL-Wavelet can be straightforwardly integrated as pre-processing steps in hyperbolic graph convolutional networks (HGCN) [Chami et al., 2019, Dai et al., 2021], improving link prediction (LP) and node classification (NC) tasks in graph learning problems. In hierarchical graph learning problems, the hierarchical structure of the nodes (i.e., samples) is given and represented by $H = ([n], E, \mathbf{A}, \mathbf{X})$, while the hierarchical structure of the node features is implicitly assumed. In HGCN, high-dimensional node features $\{\mathbf{X}_{i,:} \in \mathbb{R}^m\}_{i=1}^n$ are first embedded into a high-dimensional hyperbolic space at the origin using the exponential map. Then, these hyperbolic embeddings are mapped from one layer to the next through feature transformations learned during training. Based on the hierarchical relationships between nodes in H , the embeddings are aggregated and then passed through nonlinear activation at each layer. We refer to App. A for more details on HGCN.

In HGCN, the hierarchical structure of the samples is determined by H . In our approach, however, when a hierarchical structure is given for one mode of the dataset, it can be used as a prior for CoHSL and CoHSL-Wavelet. Specifically, we use the given hierarchical distance d_H to compute the initial \mathbf{M}_r in Alg. 1 and Alg. 2. Once CoHSL and CoHSL-Wavelet converge, we integrate our methods with HGCN as follows. Rather than mapping the Euclidean node features to hyperbolic space via the exponential map, we employ the multi-scale hyperbolic embedding [Lin et al., 2023] in $\mathbb{H}^{n+1} \times \dots \times \mathbb{H}^{n+1}$ obtained by CoHSL and CoHSL-Wavelet after convergence as the hyperbolic node representation (see App. D for details). The feature transformation is employed in the same manner as described in Dai et al. [2021]. In the neighborhood aggregation step, the learned tree from CoHSL and CoHSL-Wavelet is viewed as the inferred hierarchical structure and utilized for gathering neighborhood information. The non-linear activation function is then applied as before. We refer to the integration of CoHSL and CoHSL-Wavelet into HGCN as HGCN-CoHSL and HGCN-CoHSL-Wavelet, respectively.

6 Experimental Results

We evaluate our CoHSL and CoHSL-Wavelet on sparse approximation and unsupervised Wasserstein distance learning tasks using word-document and scRNA-seq data. Additionally, we integrate our methods into hyperbolic graph convolutional networks to validate their empirical benefits in link prediction and node classification tasks for hierarchical graph data. The implementation details, including hyperparameters, are in App. D. Additional experiments, e.g., empirical convergence, ablation study, runtime analysis, and co-clustering performance, are presented in App. E.

	Word-Document Data				scRNA-seq Data	
	BBCSPORT	TWITTER	CLASSIC	AMAZON	ZEISEL	CBMC
Co-Quadtree	26.6 / 27.8	59.5 / 24.9	64.3 / 108.7	87.3 / 102.7	157.0 / 242.4	1616.6 / 77.3
Co-Flowtree	27.4 / 31.5	69.1 / 20.9	73.7 / 97.5	88.1 / 110.1	173.7 / 240.0	1688.8 / 81.7
Co-WCTWD	26.5 / 26.7	57.6 / 17.1	63.3 / 81.7	77.4 / 96.4	136.4 / 202.9	1308.1 / 68.4
Co-WQTWD	25.2 / 32.1	56.9 / 30.2	61.3 / 100.1	74.7 / 111.0	135.0 / 224.8	1324.8 / 67.4
Co-UltraTree	37.6 / 32.1	69.8 / 18.8	76.0 / 125.5	86.3 / 133.3	155.4 / 226.6	1450.0 / 82.2
Co-TSWD-1	26.0 / 29.6	70.1 / 15.0	69.8 / 91.6	100.4 / 111.2	179.5 / 211.5	1716.1 / 79.5
Co-TSWD-5	30.5 / 24.7	58.9 / 16.0	65.7 / 98.0	83.3 / 102.3	170.2 / 234.7	1560.2 / 70.7
Co-TSWD-10	21.1 / 34.5	52.6 / 23.6	59.3 / 140.8	74.5 / 135.8	141.4 / 229.7	1373.3 / 81.2
Co-SWCTWD	35.0 / 29.5	69.0 / 24.7	79.8 / 93.6	95.9 / 104.6	170.4 / 215.9	1595.0 / 89.7
Co-SWQTWD	33.5 / 25.6	57.6 / 13.9	61.3 / 86.0	77.0 / 98.9	141.8 / 209.6	1369.8 / 68.0
Co-MST-TWD	30.4 / 34.1	69.1 / 22.1	77.5 / 109.3	97.0 / 126.4	179.1 / 254.0	1755.3 / 83.7
Co-TR-TWD	36.8 / 24.5	59.1 / 15.2	66.1 / 94.7	82.2 / 102.3	124.6 / 238.6	926.8 / 68.8
Co-HHC-TWD	22.5 / 22.7	51.5 / 13.6	58.7 / 93.3	74.1 / 110.1	192.1 / 215.5	1148.8 / 79.0
Co-gHHC-TWD	27.9 / 10.6	65.0 / 16.7	72.8 / 112.9	88.5 / 115.5	162.7 / 240.7	1612.8 / 70.8
Co-UltraFit-TWD	22.5 / 22.1	51.9 / 13.4	58.4 / 81.3	73.1 / 92.8	133.7 / 202.0	1294.6 / 78.1
QUE	22.8 / 19.8	57.8 / 10.4	71.6 / 67.6	88.8 / 72.0	93.1 / 173.3	906.4 / 58.5
CoHSL (Ours)	<u>12.9</u> / <u>7.0</u>	<u>25.4</u> / <u>3.7</u>	<u>40.4</u> / <u>24.6</u>	<u>51.0</u> / <u>30.1</u>	<u>64.4</u> / <u>110.8</u>	<u>511.3</u> / <u>50.1</u>
CoHSL-Wavelet (Ours)	10.1 / 4.8	22.4 / 3.4	37.2 / 19.4	46.6 / 26.6	50.9 / 93.7	489.4 / 45.6

Table 1: The L_1 norm of the Haar coefficient expansion. Values are reported in the format samples / features (the lowest in bold and the second lowest underlined).

6.1 Sparse Approximation for Data Organization

We first demonstrate the advantages of the tree representation obtained by the proposed CoHSL and CoHSL-Wavelet for sparse approximation tasks. The quality of the feature tree (and similarly, the sample tree) is evaluated by the L_1 norm of the Haar coefficient expansion of the samples $\|\mathbf{X}\Psi_\Omega\|_1$ in Eq. (7) (and the features, respectively) [Starck et al., 2010, Cohen et al., 2001, Candès et al., 2006]. A lower L_1 norm indicates a more efficient (sparser) representation of the data using fewer significant Haar coefficients [Gavish et al., 2010, Gavish and Coifman, 2012], thus indicating the learned tree structure better reflects the hierarchical structure of the data. We refer to App. A for more details on the L_1 norm of the Haar coefficient. We test four word-document benchmarks [Kusner et al., 2015]: BBCSPORT, TWITTER, CLASSIC, and AMAZON, and two scRNA-seq datasets [Dumitrascu et al., 2021]: ZEISEL and CBMC. For more details on these datasets, refer to App. D.

We compare CoHSL and CoHSL-Wavelet with TWD methods. For a fair comparison, we incorporate each competing method into the iterative framework. We start by using the competing method to generate an initial sample TWD matrix, which is then used to construct the sample tree by that method. This sample tree is used to calculate the feature TWD matrix, which in turn builds the feature tree. This way, throughout the iterations, the same competing TWD method computes the coupled TWDs. The competing TWD methods include: Quadtree [Indyk and Thaper, 2003], Flowtree [Backurs et al., 2020], tree-sliced Wasserstein distance (TSWD) [Le et al., 2019], UltraTree [Chen et al., 2024], weighted cluster TWD (WCTWD) [Yamada et al., 2022], weighted Quadtree TWD (WQTWD) [Yamada et al., 2022], their sliced variants SWCTWD and SWQTWD [Yamada et al., 2022], MST [Prim, 1957], Tree Representation (TR) [Sonthalia and Gilbert, 2020], gradient-based hierarchical clustering (HC) in hyperbolic space (gHHC) [Monath et al., 2019], gradient-based Ultrametric Fitting (UltraFit) [Chierchia and Perret, 2019], HC by hyperbolic Dasgupta’s cost (HHC) [Chami et al., 2020], and trees by a diffusion embedding (QUE) [Ankenman, 2014]. See App. B for details on these methods. We use the prefix “co-” with these TWDs to indicate that the trees are iteratively refined through our iterative framework.

Tab. 1 presents the L_1 norm of the Haar coefficients. We report the L_1 norm after convergence for our methods, and for the competing methods, we either report the L_1 norm after convergence or, if convergence is not achieved, the obtained value after 25 iterations. We see that CoHSL and CoHSL-Wavelet provide a more efficient sparse

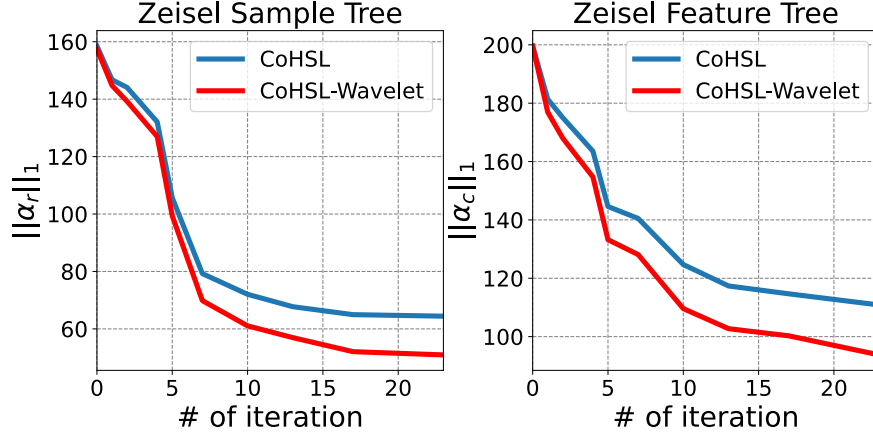


Figure 2: The L_1 norm of the Haar coefficients from the sample tree (left) and the feature tree (right) during the sparse approximation task across iterations on the ZEISEL dataset.

representation of the data, demonstrating that the sparsity and quality of the trees produced by our methods are superior and outperform those generated by the competing methods. Fig. 2 shows the L_1 norm of the Haar expansion coefficients obtained by CoHSL and CoHSL-Wavelet across iterations on the ZEISEL dataset, where we observe that the L_1 norm is iteratively reduced and reaches convergence. Note that this is not the objective we are minimizing in our CoHSL algorithm but a consequence of our method of learning a good coupled hierarchical representation of the data. The L_1 norm of the Haar coefficients obtained by the competing methods across iterations is shown in Fig. 4 in App. E. There, we observe that the competing methods demonstrate some improvement, but it is not consistent across iterations. While a few of them achieve convergence, the L_1 norm after convergence is higher compared to that of our methods.

6.2 Unsupervised Wasserstein Distance Learning

We further evaluate the TWDs produced by CoHSL and CoHSL-Wavelet on document and cell classification tasks. For a fair comparison, we evaluate the TWDs obtained by our methods against existing TWD methods within the same iterative framework, as described in Sec. 6.1. In addition, we include Wasserstein singular vectors (WSV) [Huizing et al., 2022] as a baseline, where the Wasserstein distance between samples (resp. features) serves as a ground metric to compute the Wasserstein distance for features (resp. samples). Note that WSV does not involve any tree structure. Classification is performed using k NN based on distance dissimilarity, with cross-validation over five trials. Each trial randomly splits the dataset into 70% training and 30% testing sets.

Tab. 2 shows the average document and cell classification accuracy. As in Sec. 6.1, the classification accuracy is based on the TWDs obtained by CoHSL and CoHSL-Wavelet after convergence. For the competing methods, the accuracy is reported either based on the distance obtained after convergence or the distance after 25 iterations if convergence is not achieved. We see that our methods outperform the baselines by a large margin. This indicates that the coupled TWDs effectively capture the interplay of the hierarchical structures between rows and columns. We report the classification accuracy across iterations in Fig. 5 in App. E. There, we see that the iterative process improves classification accuracy across iterations for both CoHSL and CoHSL-Wavelet. In addition, our methods demonstrate empirical convergence. While the competing TWD methods also show improvement through the iterative procedure, our methods consistently achieve better performance. Both CoHSL and CoHSL-Wavelet exhibit fast convergence, typically within 10-14 iterations in all the tested datasets.

6.3 Link Prediction and Node Classification

We test HGCN-CoHSL and HGCN-CoHSL-Wavelet on link prediction (LP) and node classification (NC) tasks. For LP task, we use a Fermi-Dirac decoder [Krioukov et al., 2010, Nickel and Kiela, 2017] to compute probability scores for edges. Then, HGCN-CoHSL and HGCN-CoHSL-Wavelet are trained by minimizing cross-entropy loss with negative sampling. The performance of LP is assessed by measuring the area under the ROC curve (AUC). For NC task, we

	Word-Document Data				scRNA-seq Data	
	BBCSPORT	TWITTER	CLASSIC	AMAZON	ZEISEL	CBMC
Co-Quadtree	96.2±0.4	69.6±0.3	95.9±0.2	89.4±0.2	81.7±1.0	80.7±0.3
Co-Flowtree	95.7±0.9	71.5±0.7	95.6±0.5	91.4±0.4	84.3±0.7	83.0±1.2
Co-WCTWD	93.2±1.2	70.2±2.1	94.7±2.6	87.4±1.0	82.5±2.9	79.4±2.1
Co-WQTWD	95.7±1.8	70.7±2.2	95.5±1.3	88.2±2.1	82.3±3.1	80.5±2.8
Co-UltraTree	95.3±1.4	70.1±2.8	93.6±2.0	86.5±2.8	85.8±1.1	84.6±1.3
Co-TSWD-1	88.2±1.4	70.4±1.2	94.7±0.9	86.1±0.5	80.2±1.4	73.2±1.0
Co-TSWD-5	88.7±1.7	71.0±1.5	96.7±0.8	91.5±0.4	82.0±0.9	75.4±0.7
Co-TSWD-10	89.2±1.1	71.4±1.8	95.5±0.2	91.8±0.7	83.8±0.5	77.2±0.9
Co-SWCTWD	93.5±2.4	70.5±1.0	94.4±1.3	90.7±1.5	82.7±1.7	79.0±0.9
Co-SWQTWD	96.2±1.2	72.4±2.1	96.0±1.1	90.6±2.3	82.4±1.4	81.3±1.1
Co-MST-TWD	88.7±2.4	68.4±3.3	91.3±2.9	87.1±1.4	80.1±2.8	76.5±1.3
Co-TR-TWD	89.5±1.2	70.9±1.7	93.4±2.2	89.5±1.4	80.7±0.8	78.5±0.9
Co-HHC-TWD	86.1±2.1	70.1±1.3	93.6±1.5	88.5±0.5	83.2±1.4	77.6±0.8
Co-gHHC-TWD	84.0±2.0	70.4±1.6	90.7±1.7	87.2±1.9	79.9±1.4	84.2±1.2
Co-UltraFit-TWD	86.8±0.9	70.9±1.1	91.9±1.0	89.9±2.0	83.7±2.9	79.1±1.8
QUE	84.7±0.5	72.4±0.6	91.9±0.5	91.6±0.9	83.6±1.4	82.5±1.9
WSV	85.9±1.0	71.4±1.3	92.6±0.7	89.0±1.5	81.6±2.4	77.5±1.7
CoHSL (Ours)	<u>96.7±0.3</u>	<u>74.1±0.5</u>	<u>97.3±0.2</u>	<u>94.0±0.4</u>	<u>90.1±0.4</u>	<u>86.7±0.5</u>
CoHSL-Wavelet (Ours)	97.3±0.5	76.7±0.7	97.6±0.1	94.2±0.2	94.0±0.6	93.3±0.7

Table 2: Document and cell classification accuracy (the highest in bold and the second highest underlined).

employ a centroid-based classification method [Liu et al., 2019], where softmax classifiers and cross-entropy loss functions are utilized. Additionally, an LP regularization objective is integrated into the NC task following Chami et al. [2019], Dai et al. [2021]. The NC task is evaluated using the F1 score for binary-class datasets and accuracy for multi-class datasets.

We conduct experiments on two citation networks, the CORA and PUBMED datasets [Sen et al., 2008, Yang et al., 2016], and the DISEASE and AIRPOT datasets from Chami et al. [2019]. Descriptions of these datasets and their splits are included in App. D. We compare our models with two shallow methods: Euclidean embedding (EUC) and Poincaré embedding (HYP) [Nickel and Kiela, 2017]. We also include comparisons with the concatenation of shallow embeddings and node features, denoted as EUC-MIXED and HYP-MIXED. Furthermore, we include multi-layer perceptron (MLP) and its hyperbolic extension, hyperbolic neural networks (HNN) [Ganea et al., 2018], as well as four graph neural networks (GNNs): GCN [Kipf and Welling, 2016], GAT [Veličković et al., 2017], GRAPH SAGE [Hamilton et al., 2017], and SGC [Wu et al., 2019]. Lastly, we include two hyperbolic counterparts: HGCN [Chami et al., 2019] and H2H-GCN [Dai et al., 2021].

Tab. 3 shows the performance of our methods on the LP and NC tasks compared to the competing methods. We repeat the random split process 10 times and report the average performance and standard deviation. Our methods consistently outperform the baselines, including GNNs and existing hyperbolic approaches, across both tasks. Notably, the HGCN-CoHSL-Wavelet model demonstrates superior performance by a significant margin across both tasks. This indicates that HGCN-CoHSL-Wavelet effectively captures the underlying coupled hierarchical information, improving the expressiveness of both GNNs and hyperbolic embeddings. We note that CoHSL and CoHSL-Wavelet could have been integrated with HGCN in other ways. However, as shown in Tab. 3, the straightforward integration presented in HGCN-CoHSL and HGCN-CoHSL-Wavelet already yields favorable results. Thus, we opt to explore more complex integration methods for future work.

	DISEASE		AIRPORT		PUBMED		CORA	
	LP	NC	LP	NC	LP	NC	LP	NC
Euc	59.8±2.0	32.5±1.1	92.0±0.0	60.9±3.4	83.3±0.1	48.2±0.7	82.5±0.3	23.8±0.7
Hyp	63.5±0.6	45.5±3.3	94.5±0.0	70.2±0.1	87.5±0.1	68.5±0.3	87.6±0.2	22.0±1.5
Euc-MIXED	49.6±1.1	35.2±3.4	91.5±0.1	68.3±2.3	86.0±1.3	63.0±0.3	84.4±0.2	46.1±0.4
Hyp-MIXED	55.1±1.3	56.9±1.5	93.3±0.0	69.6±0.1	83.8±0.3	73.9±0.2	85.6±0.5	45.9±0.3
MLP	72.6±0.6	28.8±2.5	89.8±0.5	68.6±0.6	84.1±0.9	72.4±0.2	83.1±0.5	51.5±1.0
HNN	75.1±0.3	41.0±1.8	90.8±0.2	80.5±0.5	94.9±0.1	69.8±0.4	89.0±0.1	54.6±0.4
GCN	64.7±0.5	69.7±0.4	89.3±0.4	81.4±0.6	91.1±0.5	78.1±0.2	90.4±0.2	81.3±0.3
GAT	69.8±0.3	70.4±0.4	90.5±0.3	81.5±0.3	91.2±0.1	79.0±0.3	93.7±0.1	83.0±0.7
GRAPHSAGE	65.9±0.3	69.1±0.6	90.4±0.5	82.1±0.5	86.2±1.0	77.4±2.2	85.5±0.6	77.9±2.4
SGC	65.1±0.2	69.5±0.2	89.8±0.3	80.6±0.1	94.1±0.0	78.9±0.0	91.5±0.1	81.0±0.1
HGCN	90.8±0.3	74.5±0.9	<u>96.4±0.1</u>	<u>90.6±0.2</u>	96.3±0.0	80.3±0.3	92.9±0.1	79.9±0.2
H2H-GCN	97.0±0.3	<u>88.6±1.7</u>	<u>96.4±0.1</u>	89.3±0.5	<u>96.9±0.0</u>	79.9±0.5	<u>95.0±0.0</u>	82.8±0.4
HGCN-CoHSL (Ours)	93.2±0.6	87.9±0.7	93.7±0.2	89.9±0.4	94.1±0.7	81.7±0.2	93.1±0.1	<u>82.9±0.3</u>
HGCN-CoHSL-Wavelet (Ours)	98.4±0.4	89.4±0.3	97.2±0.1	92.1±0.3	97.2±0.2	83.6±0.4	96.9±0.3	83.9±0.2

Table 3: ROC AUC for link prediction (LP), F1 score for the DISEASE dataset, and accuracy for the AIRPORT, PUBMED, and CORA datasets for node classification (NC) tasks (the highest in bold and the second highest underlined).

7 Conclusions

We present the CoHSL and its Haar wavelet-enhanced variant for learning the underlying hierarchical structures in both samples and features. The novelty of our method lies in its iteration between two “symmetric” components: 1) we use a feature tree to compute a sample TWD, and 2) we use a sample tree to compute a feature TWD. Each tree, representing samples or features, is constructed in hyperbolic space to capture the inherent hierarchy within samples or features based on the respective TWD. Through iterative refinement, where the sample and feature TWDs are successively updated, our method converges to coupled TWD matrices that respect the intrinsic correlation within the hierarchical structure of both samples and features. We demonstrate the effectiveness of our approach in sparse approximation and unsupervised Wasserstein distance learning. Additionally, we show its utility for hierarchical graph learning in node classification and link prediction tasks, where it consistently outperforms competing baselines.

Limitation and Future Work. Our method is designed for data matrices with latent hierarchical structures in both samples and features. However, it does not apply to other types of manifold data. Future work will explore other manifold components and extend the approach to tensor data.

Acknowledgments

The work of YEL and RT was supported by the European Union’s Horizon 2020 research and innovation programme under grant agreement No. 802735-ERC-DIFFOP.

References

- Yong-Yeol Ahn, James P Bagrow, and Sune Lehmann. Link communities reveal multiscale complexity in networks. *nature*, 466(7307):761–764, 2010.
- Takuya Akiba, Shotaro Sano, Toshihiko Yanase, Takeru Ohta, and Masanori Koyama. Optuna: A next-generation hyperparameter optimization framework. In *Proceedings of the 25th ACM SIGKDD international conference on knowledge discovery & data mining*, pages 2623–2631, 2019.
- Roy M Anderson and Robert M May. *Infectious diseases of humans: dynamics and control*. Oxford university press, 1991.

- Jerrod Isaac Ankenman. *Geometry and analysis of dual networks on questionnaires*. Yale University, 2014.
- Arturs Backurs, Yihe Dong, Piotr Indyk, Ilya Razenshteyn, and Tal Wagner. Scalable nearest neighbor search for optimal transport. In *International Conference on Machine Learning*, pages 497–506. PMLR, 2020.
- Alan F Beardon. *The geometry of discrete groups*, volume 91. Springer Science & Business Media, 2012.
- Mikhail Belkin and Partha Niyogi. Towards a theoretical foundation for Laplacian-based manifold methods. *Journal of Computer and System Sciences*, 74(8):1289–1308, 2008.
- Riccardo Bellazzi, Andrea Codegani, Stefano Gualandi, Giovanna Nicora, and Eleonora Vercesi. The gene mover’s distance: Single-cell similarity via optimal transport. *arXiv preprint arXiv:2102.01218*, 2021.
- Gregory Beylkin, Ronald Coifman, and Vladimir Rokhlin. Fast wavelet transforms and numerical algorithms i. *Communications on pure and applied mathematics*, 44(2):141–183, 1991.
- John Adrian Bondy and Uppaluri Siva Ramachandra Murty. *Graph theory*. Springer Publishing Company, Incorporated, 2008.
- Clément Bonet, Laetitia Chapel, Lucas Drumetz, and Nicolas Courty. Hyperbolic sliced-Wasserstein via geodesic and horospherical projections. In *Topological, Algebraic and Geometric Learning Workshops 2023*, pages 334–370. PMLR, 2023a.
- Clément Bonet, Benoit Malézieux, Alain Rakotomamonjy, Lucas Drumetz, Thomas Moreau, Matthieu Kowalski, and Nicolas Courty. Sliced-wasserstein on symmetric positive definite matrices for m/eeg signals. In *International Conference on Machine Learning*, pages 2777–2805. PMLR, 2023b.
- Nicolas Bonneel, Michiel Van De Panne, Sylvain Paris, and Wolfgang Heidrich. Displacement interpolation using Lagrangian mass transport. In *Proceedings of the 2011 SIGGRAPH Asia conference*, pages 1–12, 2011.
- Nicolas Bonneel, Julien Rabin, Gabriel Peyré, and Hanspeter Pfister. Sliced and radon wasserstein barycenters of measures. *Journal of Mathematical Imaging and Vision*, 51:22–45, 2015.
- Brian Hayward Bowditch. A course on geometric group theory. *mathematical society of japan, tokyo, 2006. MR2243589 (2007e: 20085)*, 16, 2007.
- Martin R Bridson and André Haefliger. *Metric spaces of non-positive curvature*, volume 319. Springer Science & Business Media, 2013.
- Luitzen Egbertus Jan Brouwer. Über abbildung von mannigfaltigkeiten. *Mathematische annalen*, 71(1):97–115, 1911.
- Deng Cai, Xiaofei He, Xiaoyun Wu, and Jiawei Han. Non-negative matrix factorization on manifold. In *2008 eighth IEEE international conference on data mining*, pages 63–72. IEEE, 2008.
- Emmanuel J Candès, Justin Romberg, and Terence Tao. Robust uncertainty principles: Exact signal reconstruction from highly incomplete frequency information. *IEEE Transactions on information theory*, 52(2):489–509, 2006.
- Ines Chami, Zhitao Ying, Christopher Ré, and Jure Leskovec. Hyperbolic graph convolutional neural networks. *Advances in Neural Information Processing Systems*, 32, 2019.
- Ines Chami, Albert Gu, Vaggos Chatziafratis, and Christopher Ré. From trees to continuous embeddings and back: Hyperbolic hierarchical clustering. *Advances in Neural Information Processing Systems*, 33:15065–15076, 2020.
- Jonathan Chang and David M Blei. Hierarchical relational models for document networks. 2010.
- Samantha Chen, Puoya Tabaghi, and Yusu Wang. Learning ultrametric trees for optimal transport regression. In *Proceedings of the AAAI Conference on Artificial Intelligence*, volume 38, pages 20657–20665, 2024.
- Eric C Chi and Kenneth Lange. Splitting methods for convex clustering. *Journal of Computational and Graphical Statistics*, 24(4):994–1013, 2015.

- Eric C Chi and Stefan Steinerberger. Recovering trees with convex clustering. *SIAM Journal on Mathematics of Data Science*, 1(3):383–407, 2019.
- Eric C Chi, Genevera I Allen, and Richard G Baraniuk. Convex biclustering. *Biometrics*, 73(1):10–19, 2017.
- Giovanni Chierchia and Benjamin Perret. Ultrametric fitting by gradient descent. *Advances in neural information processing systems*, 32, 2019.
- Lenaic Chizat, Pierre Roussillon, Flavien Léger, François-Xavier Vialard, and Gabriel Peyré. Faster Wasserstein distance estimation with the Sinkhorn divergence. *Advances in Neural Information Processing Systems*, 33:2257–2269, 2020.
- Aaron Clauset, Cristopher Moore, and Mark EJ Newman. Hierarchical structure and the prediction of missing links in networks. *Nature*, 453(7191):98–101, 2008.
- Albert Cohen, Wolfgang Dahmen, Ingrid Daubechies, and Ronald DeVore. Tree approximation and optimal encoding. *Applied and Computational Harmonic Analysis*, 11(2):192–226, 2001.
- Ronald R Coifman and Stéphane Lafon. Diffusion maps. *Applied and computational harmonic analysis*, 21(1):5–30, 2006.
- Thomas H Cormen, Charles E Leiserson, Ronald L Rivest, and Clifford Stein. *Introduction to algorithms*. MIT press, 2022.
- Trevor F Cox and Michael AA Cox. *Multidimensional scaling*. CRC press, 2000.
- Marco Cuturi. Sinkhorn distances: Lightspeed computation of optimal transport. *Advances in Neural Information Processing Systems*, 26, 2013.
- Kostadin Dabov, Alessandro Foi, Vladimir Katkovnik, and Karen Egiazarian. Image denoising by sparse 3-d transform-domain collaborative filtering. *IEEE Transactions on image processing*, 16(8):2080–2095, 2007.
- Jindou Dai, Yuwei Wu, Zhi Gao, and Yunde Jia. A hyperbolic-to-hyperbolic graph convolutional network. In *Proceedings of the IEEE/CVF Conference on Computer Vision and Pattern Recognition*, pages 154–163, 2021.
- Ingrid Daubechies. The wavelet transform, time-frequency localization and signal analysis. *IEEE transactions on information theory*, 36(5):961–1005, 1990.
- Minh N Do and Martin Vetterli. The contourlet transform: an efficient directional multiresolution image representation. *IEEE Transactions on image processing*, 14(12):2091–2106, 2005.
- Bianca Dumitrescu, Soledad Villar, Dustin G Mixon, and Barbara E Engelhardt. Optimal marker gene selection for cell type discrimination in single cell analyses. *Nature communications*, 12(1):1–8, 2021.
- David K Duvenaud, Dougal Maclaurin, Jorge Iparraguirre, Rafael Bombarell, Timothy Hirzel, Alán Aspuru-Guzik, and Ryan P Adams. Convolutional networks on graphs for learning molecular fingerprints. *Advances in neural information processing systems*, 28, 2015.
- Steven N Evans and Frederick A Matsen. The phylogenetic Kantorovich–Rubinstein metric for environmental sequence samples. *Journal of the Royal Statistical Society Series B: Statistical Methodology*, 74(3):569–592, 2012.
- Charles Fefferman, Sanjoy Mitter, and Hariharan Narayanan. Testing the manifold hypothesis. *Journal of the American Mathematical Society*, 29(4):983–1049, 2016.
- Bruno Cesar Feltes, Eduardo Bassani Chandelier, Bruno Iochins Grisci, and Marcio Dorn. Cumida: an extensively curated microarray database for benchmarking and testing of machine learning approaches in cancer research. *Journal of Computational Biology*, 26(4):376–386, 2019.
- Chakib Fattal, Iazhar Labiod, and Mohamed Nadif. Efficient and effective optimal transport-based biclustering. In Alice H. Oh, Alekh Agarwal, Danielle Belgrave, and Kyunghyun Cho, editors, *Advances in Neural Information Processing Systems*, 2022.

- Rémi Flamary, Nicolas Courty, Alexandre Gramfort, Mokhtar Z Alaya, Aurélie Boisbunon, Stanislas Chambon, Laetitia Chapel, Adrien Corenflos, Kilian Fatras, Nemo Fournier, et al. Pot: Python optimal transport. *The Journal of Machine Learning Research*, 22(1):3571–3578, 2021.
- Maurice Fréchet. Les éléments aléatoires de nature quelconque dans un espace distancié. In *Annales de l’institut Henri Poincaré*, volume 10, pages 215–310, 1948.
- Jerome H Friedman, Trevor Hastie, and Rob Tibshirani. Regularization paths for generalized linear models via coordinate descent. *Journal of statistical software*, 33:1–22, 2010.
- Octavian Ganea, Gary Bécigneul, and Thomas Hofmann. Hyperbolic neural networks. *Advances in Neural Information Processing Systems*, 31, 2018.
- Matan Gavish and Ronald R Coifman. Sampling, denoising and compression of matrices by coherent matrix organization. *Applied and Computational Harmonic Analysis*, 33(3):354–369, 2012.
- Matan Gavish, Boaz Nadler, and Ronald R Coifman. Multiscale wavelets on trees, graphs and high dimensional data: Theory and applications to semi supervised learning. In *ICML*, 2010.
- Justin Gilmer, Samuel S Schoenholz, Patrick F Riley, Oriol Vinyals, and George E Dahl. Neural message passing for quantum chemistry. In *International conference on machine learning*, pages 1263–1272. PMLR, 2017.
- Gérard Govaert and Mohamed Nadif. Block clustering with bernoulli mixture models: Comparison of different approaches. *Computational Statistics & Data Analysis*, 52(6):3233–3245, 2008.
- Alfred Haar. Zur theorie der orthogonalen funktionensysteme. *Mathematische Annalen*, 71(1):38–53, 1911.
- Will Hamilton, Zhitao Ying, and Jure Leskovec. Inductive representation learning on large graphs. *Advances in Neural Information Processing Systems*, 30, 2017.
- John A Hartigan and Manchek A Wong. Algorithm AS 136: A k-means clustering algorithm. *Journal of the royal statistical society. series c (applied statistics)*, 28(1):100–108, 1979.
- Seunghoon Hong, Xinchun Yan, Thomas S Huang, and Honglak Lee. Learning hierarchical semantic image manipulation through structured representations. *Advances in Neural Information Processing Systems*, 31, 2018.
- Roger A Horn and Charles R Johnson. *Matrix analysis*. Cambridge university press, 2012.
- Reiner Horst and Hoang Tuy. *Global optimization: Deterministic approaches*. Springer Science & Business Media, 2013.
- Gao Huang, Chuan Guo, Matt J Kusner, Yu Sun, Fei Sha, and Kilian Q Weinberger. Supervised word mover’s distance. *Advances in Neural Information Processing Systems*, 29, 2016.
- Lawrence Hubert and Phipps Arabie. Comparing partitions. *Journal of classification*, 2(1):193–218, 1985.
- Geert-Jan Huizing, Laura Cantini, and Gabriel Peyré. Unsupervised ground metric learning using Wasserstein singular vectors. In *International Conference on Machine Learning*, pages 9429–9443. PMLR, 2022.
- Piotr Indyk and Nitin Thaper. Fast image retrieval via embeddings. In *3rd international workshop on statistical and computational theories of vision*, 2, 2003.
- Konrad Iwanicki and Maarten van Steen. On hierarchical routing in wireless sensor networks. In *2009 International Conference on Information Processing in Sensor Networks*, pages 133–144. IEEE, 2009.
- Pablo A Jaskowiak, Ricardo JGB Campello, and Ivan G Costa. On the selection of appropriate distances for gene expression data clustering. In *BMC bioinformatics*, volume 15, pages 1–17. Springer, 2014.
- Leonid V Kantorovich. On the translocation of masses. In *Dokl. Akad. Nauk. USSR (NS)*, volume 37, pages 199–201, 1942.
- Tom Kenter and Maarten De Rijke. Short text similarity with word embeddings. In *Proceedings of the 24th ACM international on conference on information and knowledge management*, pages 1411–1420, 2015.

- Joe Kileel, Amit Moscovich, Nathan Zelesko, and Amit Singer. Manifold learning with arbitrary norms. *Journal of Fourier Analysis and Applications*, 27(5):82, 2021.
- Thomas N Kipf and Max Welling. Semi-supervised classification with graph convolutional networks. In *International Conference on Learning Representations*, 2016.
- Soheil Kolouri, Kimia Nadjahi, Umut Simsekli, Roland Badeau, and Gustavo Rohde. Generalized sliced wasserstein distances. *Advances in neural information processing systems*, 32, 2019.
- Dmitri Krioukov, Fragkiskos Papadopoulos, Maksim Kitsak, Amin Vahdat, and Marián Boguná. Hyperbolic geometry of complex networks. *Physical Review E—Statistical, Nonlinear, and Soft Matter Physics*, 82(3):036106, 2010.
- Matt Kusner, Yu Sun, Nicholas Kolkin, and Kilian Weinberger. From word embeddings to document distances. In *International Conference on Machine Learning*, pages 957–966. PMLR, 2015.
- Charlotte Laclau, Ievgen Redko, Basarab Matei, Younes Bennani, and Vincent Brault. Co-clustering through optimal transport. In *International Conference on Machine Learning*, pages 1955–1964. PMLR, 2017.
- Tam Le, Makoto Yamada, Kenji Fukumizu, and Marco Cuturi. Tree-sliced variants of Wasserstein distances. *Advances in Neural Information Processing Systems*, 32, 2019.
- William Leeb and Ronald Coifman. Hölder–Lipschitz norms and their duals on spaces with semigroups, with applications to earth mover’s distance. *Journal of Fourier Analysis and Applications*, 22(4):910–953, 2016.
- Elizabeth A Leicht and Mark EJ Newman. Community structure in directed networks. *Physical review letters*, 100(11):118703, 2008.
- Ya-Wei Eileen Lin, Yuval Kluger, and Ronen Talmon. Hyperbolic Procrustes analysis using Riemannian geometry. *Advances in Neural Information Processing Systems*, 34:5959–5971, 2021.
- Ya-Wei Eileen Lin, Ronald R. Coifman, Gal Mishne, and Ronen Talmon. Hyperbolic diffusion embedding and distance for hierarchical representation learning. In *International Conference on Machine Learning*, pages 21003–21025. PMLR, 2023.
- Ya-Wei Eileen Lin, Ronald R. Coifman, Gal Mishne, and Ronen Talmon. Tree-Wasserstein distance for high dimensional data with a latent feature hierarchy. *arXiv preprint arXiv:2410.21107*, 2024a.
- Ya-Wei Eileen Lin, Yuval Kluger, and Ronen Talmon. Hyperbolic diffusion Procrustes analysis for intrinsic representation of hierarchical data sets. In *ICASSP 2024-2024 IEEE International Conference on Acoustics, Speech and Signal Processing (ICASSP)*, pages 6325–6329. IEEE, 2024b.
- Qi Liu, Maximilian Nickel, and Douwe Kiela. Hyperbolic graph neural networks. *Advances in Neural Information Processing Systems*, 32, 2019.
- Malte D Luecken and Fabian J Theis. Current best practices in single-cell RNA-seq analysis: a tutorial. *Molecular systems biology*, 15(6):e8746, 2019.
- Sara C Madeira and Arlindo L Oliveira. Biclustering algorithms for biological data analysis: a survey. *IEEE/ACM transactions on computational biology and bioinformatics*, 1(1):24–45, 2004.
- Stéphane Mallat. *A wavelet tour of signal processing*. Elsevier, 1999.
- Stephane G Mallat. Multiresolution approximations and wavelet orthonormal bases of $L^2(\mathbb{R})$. *Transactions of the American mathematical society*, 315(1):69–87, 1989.
- Pascal Mettes, Mina Ghadimi Atigh, Martin Keller-Ressel, Jeffrey Gu, and Serena Yeung. Hyperbolic deep learning in computer vision: A survey. *International Journal of Computer Vision*, pages 1–25, 2024.
- Tomas Mikolov, Ilya Sutskever, Kai Chen, Greg S Corrado, and Jeff Dean. Distributed representations of words and phrases and their compositionality. *Advances in Neural Information Processing Systems*, 26, 2013.

- Zeeshan Hameed Mir and Young-Bae Ko. A quadtree-based hierarchical data dissemination for mobile sensor networks. *Telecommunication Systems*, 36(1):117–128, 2007.
- Gal Mishne, Ronen Talmon, Ron Meir, Jackie Schiller, Maria Lavzin, Uri Dubin, and Ronald R Coifman. Hierarchical coupled-geometry analysis for neuronal structure and activity pattern discovery. *IEEE Journal of Selected Topics in Signal Processing*, 10(7):1238–1253, 2016.
- Gal Mishne, Ronen Talmon, Israel Cohen, Ronald R Coifman, and Yuval Kluger. Data-driven tree transforms and metrics. *IEEE transactions on signal and information processing over networks*, 4(3):451–466, 2017.
- Gal Mishne, Eric Chi, and Ronald Coifman. Co-manifold learning with missing data. In *International Conference on Machine Learning*, pages 4605–4614. PMLR, 2019.
- Nicholas Monath, Manzil Zaheer, Daniel Silva, Andrew McCallum, and Amr Ahmed. Gradient-based hierarchical clustering using continuous representations of trees in hyperbolic space. In *Proceedings of the 25th ACM SIGKDD International Conference on Knowledge Discovery & Data Mining*, pages 714–722, 2019.
- Gaspard Monge. Mémoire sur la théorie des déblais et des remblais. *Mem. Math. Phys. Acad. Royale Sci.*, pages 666–704, 1781.
- Maximillian Nickel and Douwe Kiela. Poincaré embeddings for learning hierarchical representations. *Advances in Neural Information Processing Systems*, 30, 2017.
- Maximillian Nickel and Douwe Kiela. Learning continuous hierarchies in the Lorentz model of hyperbolic geometry. In *International Conference on Machine Learning*, pages 3779–3788. PMLR, 2018.
- Gabriel Peyré, Marco Cuturi, et al. Computational optimal transport: With applications to data science. *Foundations and Trends® in Machine Learning*, 11(5-6):355–607, 2019.
- Robert Clay Prim. Shortest connection networks and some generalizations. *The Bell System Technical Journal*, 36(6): 1389–1401, 1957.
- Julien Rabin, Gabriel Peyré, Julie Delon, and Marc Bernot. Wasserstein barycenter and its application to texture mixing. In *Scale Space and Variational Methods in Computer Vision: Third International Conference, SSVM 2011, Ein-Gedi, Israel, May 29–June 2, 2011, Revised Selected Papers 3*, pages 435–446. Springer, 2012.
- John G Ratcliffe, S Axler, and KA Ribet. *Foundations of hyperbolic manifolds*, volume 149. Springer, 1994.
- Frederic Sala, Chris De Sa, Albert Gu, and Christopher Ré. Representation tradeoffs for hyperbolic embeddings. In *International Conference on Machine Learning*, pages 4460–4469. PMLR, 2018.
- Ryoma Sato, Makoto Yamada, and Hisashi Kashima. Fast unbalanced optimal transport on a tree. *Advances in Neural Information Processing Systems*, 33:19039–19051, 2020.
- Prithviraj Sen, Galileo Namata, Mustafa Bilgic, Lise Getoor, Brian Galligher, and Tina Eliassi-Rad. Collective classification in network data. *AI magazine*, 29(3):93–93, 2008.
- Eugene Seneta. *Non-negative matrices and Markov chains*. Springer Science & Business Media, 2006.
- Nauman Shahid, Nathanael Perraudin, Vassilis Kalofolias, Gilles Puy, and Pierre Vandergheynst. Fast robust pca on graphs. *IEEE Journal of Selected Topics in Signal Processing*, 10(4):740–756, 2016.
- Chao Shen and Hau-Tieng Wu. Scalability and robustness of spectral embedding: Landmark diffusion is all you need. *Information and Inference: A Journal of the IMA*, 11(4):1527–1595, 2022.
- Amit Singer. From graph to manifold Laplacian: The convergence rate. *Applied and Computational Harmonic Analysis*, 21(1):128–134, 2006.
- Rishi Sonthalia and Anna Gilbert. Tree! I am no Tree! I am a low dimensional hyperbolic embedding. *Advances in Neural Information Processing Systems*, 33:845–856, 2020.

- Jean-Luc Starck, Fionn Murtagh, and Jalal M Fadili. *Sparse image and signal processing: wavelets, curvelets, morphological diversity*. Cambridge university press, 2010.
- Marlon Stoeckius, Christoph Hafemeister, William Stephenson, Brian Houck-Loomis, Pratip K Chattopadhyay, Harold Swerdlow, Rahul Satija, and Peter Smibert. Simultaneous epitope and transcriptome measurement in single cells. *Nature methods*, 14(9):865–868, 2017.
- Amos Tanay and Aviv Regev. Scaling single-cell genomics from phenomenology to mechanism. *Nature*, 541(7637):331–338, 2017.
- Vayer Titouan, Ievgen Redko, Rémi Flamary, and Nicolas Courty. Co-optimal transport. *Advances in Neural Information Processing Systems*, 33:17559–17570, 2020.
- Dmitry Ulyanov, Andrea Vedaldi, and Victor Lempitsky. Deep image prior. In *Proceedings of the IEEE conference on computer vision and pattern recognition*, pages 9446–9454, 2018.
- Petar Veličković, Guillem Cucurull, Arantxa Casanova, Adriana Romero, Pietro Lio, and Yoshua Bengio. Graph attention networks. *arXiv preprint arXiv:1710.10903*, 2017.
- Cédric Villani. *Optimal transport: old and new*, volume 338. Springer, 2009.
- Liming Wang and Xiaodong Wang. Hierarchical dirichlet process model for gene expression clustering. *EURASIP Journal on Bioinformatics and Systems Biology*, 2013:1–14, 2013.
- Xiao Wang, Houye Ji, Chuan Shi, Bai Wang, Yanfang Ye, Peng Cui, and Philip S Yu. Heterogeneous graph attention network. In *The world wide web conference, pages 2022–2032*, 2019.
- Simon Weber, Bar Zöngür, Nikita Araslanov, and Daniel Cremers. Flattening the parent bias: Hierarchical semantic segmentation in the Poincaré ball. In *Proceedings of the IEEE/CVF Conference on Computer Vision and Pattern Recognition*, pages 28223–28232, 2024.
- Stephen J Wright. Coordinate descent algorithms. *Mathematical programming*, 151(1):3–34, 2015.
- Felix Wu, Amauri Souza, Tianyi Zhang, Christopher Fifty, Tao Yu, and Kilian Weinberger. Simplifying graph convolutional networks. In *International conference on machine learning*, pages 6861–6871. PMLR, 2019.
- Zhenqin Wu, Bharath Ramsundar, Evan N Feinberg, Joseph Gomes, Caleb Geniesse, Aneesh S Pappu, Karl Leswing, and Vijay Pande. Moleculenet: a benchmark for molecular machine learning. *Chemical science*, 9(2):513–530, 2018.
- Or Yair, Ronen Talmon, Ronald R Coifman, and Ioannis G Kevrekidis. Reconstruction of normal forms by learning informed observation geometries from data. *Proceedings of the National Academy of Sciences*, 114(38):E7865–E7874, 2017.
- Makoto Yamada, Yuki Takezawa, Ryoma Sato, Han Bao, Zornitsa Kozareva, and Sujith Ravi. Approximating 1-Wasserstein distance with trees. *Transactions on Machine Learning Research*, 2022.
- Zhilin Yang, William Cohen, and Ruslan Salakhudinov. Revisiting semi-supervised learning with graph embeddings. In *International conference on machine learning*, pages 40–48. PMLR, 2016.
- Rex Ying, Ruining He, Kaifeng Chen, Pong Eksombatchai, William L Hamilton, and Jure Leskovec. Graph convolutional neural networks for web-scale recommender systems. In *Proceedings of the 24th ACM SIGKDD international conference on knowledge discovery & data mining*, pages 974–983, 2018.
- Amit Zeisel, Ana B Muñoz-Manchado, Simone Codeluppi, Peter Lönnerberg, Gioele La Manno, Anna Juréus, Sueli Marques, Hermany Munguba, Liqun He, Christer Betscholtz, et al. Cell types in the mouse cortex and hippocampus revealed by single-cell RNA-seq. *Science*, 347(6226):1138–1142, 2015.
- Yiding Zhang, Xiao Wang, Chuan Shi, Xunqiang Jiang, and Yanfang Ye. Hyperbolic graph attention network. *IEEE Transactions on Big Data*, 8(6):1690–1701, 2021.

A Additional Background

To provide further context, we include additional background information relevant to the concepts and methodologies discussed in the main text.

A.1 Hyperbolic Geometry

Hyperbolic geometry is a branch of non-Euclidean geometry that describes spaces with a constant negative curvature. It is widely used in modeling structures with hierarchical or tree-like relationships [Ratcliffe et al., 1994]. There are several models commonly used to describe hyperbolic spaces. The Poincaré disk model maps the entire hyperbolic plane inside a unit disk, with geodesics represented as arcs orthogonal to the boundary or straight lines through the center. The Poincaré half-plane model uses the upper half of the Euclidean plane, where geodesics are semicircles orthogonal to the horizontal axis or vertical lines. The Klein model represents hyperbolic space in a unit disk but sacrifices angular accuracy, making it more suitable for some specific calculations. The hyperboloid model relies on a higher-dimensional Lorentzian inner product, offering computational efficiency for applications like machine learning. In this work, we consider two equivalent models of hyperbolic space [Ratcliffe et al., 1994]: the Poincaré half-space and the hyperboloid model. The Poincaré half-space was used for embedding that reveals the hierarchical structure underlying data, while the hyperboloid model is advantageous for its simple closed-form Riemannian operations [Nickel and Kiela, 2018, Lin et al., 2021].

The d -dimensional Poincaré half-space is defined as $\mathbb{H}^d = \{\mathbf{a} \in \mathbb{R}^d \mid \mathbf{a}(d) > 0\}$ with the Riemannian metric tensor $ds^2 = (d\mathbf{a}^2(1) + \dots + d\mathbf{a}^2(d))/\mathbf{a}^2(d)$ [Beardon, 2012]. Let \mathbb{L}^d denote the hyperboloid manifold in d dimensions, defined by $\mathbb{L}^d = \{\mathbf{b} \in \mathbb{R}^{d+1} \mid \langle \mathbf{b}, \mathbf{b} \rangle_{\mathcal{L}} = -1, \mathbf{b}(1) > 0\}$, where $\langle \cdot, \cdot \rangle_{\mathcal{L}}$ is the Minkowski inner product $\langle \mathbf{b}, \mathbf{b} \rangle_{\mathcal{L}} = \mathbf{b}^\top [-1, \mathbf{0}^\top; \mathbf{0}, \mathbf{I}_d] \mathbf{b}$. Let $\mathcal{T}_{\mathbf{b}}\mathbb{L}^d$ be the tangent space at point $\mathbf{b} \in \mathbb{L}^d$, given by $\mathcal{T}_{\mathbf{b}}\mathbb{L}^d = \{\mathbf{v} \in \mathbb{R}^{d+1} \mid \langle \mathbf{v}, \mathbf{v} \rangle_{\mathcal{L}} = 0\}$. We denote $\|\mathbf{v}\|_{\mathcal{L}} = \sqrt{\langle \mathbf{v}, \mathbf{v} \rangle_{\mathcal{L}}}$ as the norm of $\mathbf{v} \in \mathcal{T}_{\mathbf{b}}\mathbb{L}^d$. For two different points $\mathbf{b}_1, \mathbf{b}_2 \in \mathbb{L}^d$ and $\mathbf{0} \neq \mathbf{v} \in \mathcal{T}_{\mathbf{b}_1}\mathbb{L}^d$, the exponential and logarithmic maps of \mathbb{L}^d are given by $\text{Exp}_{\mathbf{b}_1}(\mathbf{v}) = \cosh(\|\mathbf{v}\|_{\mathcal{L}})\mathbf{b}_1 + \sinh(\|\mathbf{v}\|_{\mathcal{L}})\mathbf{v}/\|\mathbf{v}\|_{\mathcal{L}}$ and $\text{Log}_{\mathbf{b}_1}(\mathbf{b}_2) = \cosh^{-1}(\eta)(\mathbf{b}_2 - \eta\mathbf{b}_1)/\sqrt{\eta^2 - 1}$, where $\eta = -\langle \mathbf{b}_1, \mathbf{b}_2 \rangle_{\mathcal{L}}$. The parallel transport of a vector $\mathbf{v} \in \mathcal{T}_{\mathbf{b}_1}\mathbb{L}^d$ along the geodesic path from $\mathbf{b}_1 \in \mathbb{L}^d$ to $\mathbf{b}_2 \in \mathbb{L}^d$ is given by $\text{PT}_{\mathbf{b}_1 \rightarrow \mathbf{b}_2}(\mathbf{v}) = \mathbf{v} + \frac{\langle \mathbf{b}_2 - \lambda \mathbf{b}_1, \mathbf{v} \rangle_{\mathcal{L}}}{\lambda + 1}(\mathbf{b}_1 + \mathbf{b}_2)$, where $\lambda = -\langle \mathbf{b}_1, \mathbf{b}_2 \rangle_{\mathcal{L}}$, while keeping the metric tensor unchanged. Due to the equivalence between the Poincaré half-space and the Lorentz model, there exists a diffeomorphism $\mathcal{P} : \mathbb{H}^d \rightarrow \mathbb{L}^d$ that maps points from the Poincaré half-space $\mathbf{a} \in \mathbb{H}^d$ to the Lorentz model $\mathbf{b} \in \mathbb{L}^d$ by

$$\mathbf{b} = \mathcal{P}(\mathbf{a}) = \frac{(1 + \|\mathbf{c}\|^2, 2\mathbf{c}(1), \dots, 2\mathbf{c}(d+1))}{1 - \|\mathbf{c}\|^2}, \quad (9)$$

where

$$\mathbf{c} = \frac{(2\mathbf{a}(1), \dots, 2\mathbf{a}(d), \|\mathbf{a}\|^2 - 1)}{\|\mathbf{a}\|^2 + 2\mathbf{a}(d+1) + 1}.$$

A.2 Diffusion Geometry

Diffusion geometry [Coifman and Lafon, 2006] is a mathematical framework that analyzes data by capturing intrinsic geometric structures through diffusion processes. It is rooted in the study of diffusion dynamics on graphs, manifolds, or general data spaces, where the spread of information or heat over time reflects the underlying connectivity and geometry. This approach is effective for understanding high-dimensional data by uncovering relationships that traditional methods may not easily detect. Diffusion geometry represents data as nodes in a graph and models their relationships using a diffusion operator. By simulating diffusion processes over this structure, the method identifies meaningful relationships, often based on proximity and connectivity in the space.

Consider a set of high-dimensional points $\mathcal{Z} = \{\mathbf{z}_j \in \mathbb{R}^n\}_{j=1}^m$ lying on a low-dimensional manifold. Let $\mathbb{R}^{m \times m} \ni \mathbf{K} = \exp(-\mathbf{M}^{\circ 2}/\epsilon)$ be an affinity matrix, where $\mathbf{M} \in \mathbb{R}^{m \times m}$ is a suitable pairwise distance matrix between the points $\{\mathbf{z}_j\}_{j=1}^m$, \circ is the Hadamard power, and $\epsilon > 0$ is the scale parameter. Note that the matrix \mathbf{K} can be interpreted as an undirected weighted graph $G = (\mathcal{Z}, \mathbf{K})$, where \mathcal{Z} is the node set and \mathbf{K} represents the edge weights. The diffusion operator [Coifman and Lafon, 2006] is constructed by $\mathbf{P} = \mathbf{K}\mathbf{D}^{-1}$, where \mathbf{D} is the diagonal degree matrix with entries $\mathbf{D}(j, j) = \sum_l \mathbf{K}(j, l)$. We remark that a density normalization affinity matrix can be considered to mitigate the effects of non-uniform data sampling [Coifman and Lafon, 2006]. Note that the diffusion operator \mathbf{P}

is column-stochastic, allowing it to be used as a transition probability matrix of a Markov chain on G . Specifically, the vector $\mathbf{p}_j^t = \mathbf{P}^t \delta_j \in \Delta_m$ is the propagated density after diffusion time $t \in \mathbb{R}_+$ of a density $\delta_j \in \Delta_m$ initially concentrated at point j .

The diffusion operator has been demonstrated to have favorable convergence [Coifman and Lafon, 2006]. As $m \rightarrow \infty$ and $\epsilon \rightarrow 0$, the operator $\mathbf{P}^{t/\epsilon}$ converges pointwise to the Neumann heat kernel associated with the underlying manifold. This convergence indicates that the diffusion operator can be viewed as a discrete approximation of the continuous heat kernel, thereby effectively capturing the geometric structure of the underlying manifold in a finite-dimensional setting [Coifman and Lafon, 2006, Singer, 2006, Belkin and Niyogi, 2008].

A.3 Hyperbolic Diffusion Tree Decoding

Recently, the work [Lin et al., 2023] introduced a tree construction method that recovers the latent hierarchical structure underlying data based on hyperbolic geometry and diffusion geometry. Specifically, this latent hierarchical structure can be modeled by a tree T , which can be viewed as a discretization of an underlying manifold.

Consider the diffusion operator constructed as in App. A.2, the multi-scale diffusion densities $\mu_j^k = \mathbf{P}^{2^{-k}} \delta_j \in \Delta_m$ are considered with dyadic diffusion time steps $t = 2^{-k}$ for $k \in \mathbb{Z}_0^+$, and are embedded into the Poincaré half-space by $(j, k) \mapsto \mathbf{y}_j^k = [(\tau_j^k)^\top, 2^{k/2-2}]^\top \in \mathbb{H}^{m+1}$, where $\tau_j^k = \mu_j^{k \circ 1/2}$ is the Hadamard root of μ_j^k . Note that diffusion geometry is effective in recovering the underlying manifold [Coifman and Lafon, 2006]; however, the study in Lin et al. [2023] demonstrated that considering propagated densities with diffusion times on dyadic grids can capture the hidden hierarchical structures by incorporating local information from exponentially expanding neighborhoods around each point. The multi-scale hyperbolic embedding is a function $\text{Embedding} : \mathcal{Z} \rightarrow \mathcal{M}$ defined by

$$\text{Embedding}(\mathbf{z}_j) = [(\mathbf{y}^0)^\top, (\mathbf{y}^1)^\top, \dots, (\mathbf{y}^K)^\top]^\top, \quad (10)$$

where $\mathcal{M} = \mathbb{H}^{m+1} \times \mathbb{H}^{m+1} \times \dots \times \mathbb{H}^{m+1}$ of $(K+1)$ elements. The geodesic distance induced in \mathcal{M} is the ℓ_1 distance on the product manifold \mathcal{M} , given by

$$d_{\mathcal{M}}(j, j') = \sum_{k=0}^K 2 \sinh^{-1} \left(2^{-k/2+1} \|\mathbf{y}_j^k - \mathbf{y}_{j'}^k\|_2 \right). \quad (11)$$

Theorem A.1 (Theorem 1 in Lin et al. [2023]). *For sufficiently large K , the embedding distance is bilipschitz equivalent to the underlying tree distance, i.e., $d_{\mathcal{M}} \simeq d_T$.*

The multi-scale embedding is then used for binary tree construction $\Gamma_{\mathcal{M}}$ with m leaves [Lin et al., 2024a]. Pairs of features are merged based on the Riemannian mean [Fréchet, 1948] of the radius of the geodesic connecting \mathbf{y}_j^k and $\mathbf{y}_{j'}^k$ for $k = \{0, \dots, K\}$. The hyperbolic tree decoding is summarized in Alg. 3.

Theorem A.2 (Theorem 1 in Lin et al. [2024a]). *For sufficiently large K and m , the tree metric d_B in Alg. 3 is bilipschitz equivalent to the underlying tree metric d_T , where T is the ground truth latent tree and d_T is the hidden tree metric between features defined as the length of the shortest path on T .*

A.4 Trees

Trees are fundamental structures in graph theory. A tree is a type of graph characterized by hierarchical organization and efficient traversal properties. Below, we outline key concepts and definitions that provide a foundational understanding of trees and their associated metrics.

Graph and Shortest Path Metric. A graph $G = (V, E, \mathbf{A})$ consists of a set of nodes V , edges E , and a weight matrix $\mathbf{A} \in \mathbb{R}^{m \times m}$. For any two nodes $j, j' \in V$, the shortest path metric $d_G(j, j')$ represents the minimum sum of edge weights along any path connecting j and j' .

Tree Metrics. A metric $d : V \times V \rightarrow \mathbb{R}$ is classified as a tree metric if there exists a tree $T = (V, E, \mathbf{A})$ such that $d(j, j')$ corresponds to the shortest path metric $d_T(j, j')$ on T . Notably, tree metrics exhibit 0-hyperbolicity, making them well-suited for representing hierarchical data.

Algorithm 3 Hyperbolic Diffusion Tree Decoding [Lin et al., 2024a]

Input: Pairwise distance matrix $\mathbf{M} \in \mathbb{R}^{m \times m}$, the maximal scale K , and the scale parameter ϵ

Output: A binary tree B with m leaf nodes

```

function HyperbolicDiffusionTree( $\mathbf{M}$ )
   $\mathbf{K} \leftarrow \exp(-\mathbf{M}^{\circ 2}/\epsilon)$ 
   $\mathbf{D} \leftarrow \text{diag}(\mathbf{K})$ 
   $\mathbf{P} \leftarrow \mathbf{K}\mathbf{D}^{-1}$ 
   $\mathbf{U}\mathbf{\Lambda}\mathbf{V}^\top = \text{eig}(\mathbf{P})$ 
  for  $k \in \{0, 1, \dots, K\}$  do
     $\lambda_k \leftarrow \Lambda^{2^{-k}}$ 
    for  $j \in [m]$  do
       $\mathbf{y}_j^k \leftarrow [(\mathbf{U}\lambda_k\mathbf{V}^\top)^{\circ 1/2}\boldsymbol{\delta}_j, 2^{k/2-2}]^\top$ 
    end for
  end while
   $B \leftarrow \text{leaves}(\{j\} : j \in [m])$ 
  for  $j, j' \in [m]$  do
    for  $k \in \{0, 1, \dots, K\}$  do
       $\mathbf{o}_{j,j'}^k \leftarrow [\mathbf{0}^\top, \text{proj}(\mathbf{y}_j^k, \mathbf{y}_{j'}^k)]^\top$ 
    end for
     $\bar{\mathbf{h}}_{j,j'} \leftarrow \arg \min_{\mathbf{h} \in \mathbb{H}^{m+1}} \sum_{k=0}^K d_{\mathbb{H}^{m+1}}^2(\mathbf{h}, \mathbf{o}_{j,j'}^k)$ 
  end for
   $\mathcal{S} = \{(j, j') \mid \text{sorted by } \bar{\mathbf{h}}_{j,j'}(m+1)\}$ 
  for  $(j, j') \in \mathcal{S}$  do
    if  $j$  and  $j'$  are not in the same subtree
       $\mathcal{I}_j \leftarrow$  internal node for node  $j$ 
       $\mathcal{I}_{j'} \leftarrow$  internal node for node  $j'$ 
      add an internal node for  $\mathcal{I}_j$  and  $\mathcal{I}_{j'}$ 
      assign the geodesic edge weight
    end if
  end for
return  $B$ 

```

Binary Trees. Binary trees are a specific class of trees where each internal node has exactly two child nodes. In a balanced binary tree, internal nodes (except the root) have a degree of 3, while leaf nodes have a degree of 1. The structure of a balanced binary tree ensures efficient representation and computation. A rooted and balanced binary tree is a further refinement where one internal node, designated as the root, has a degree of 2, and all other internal nodes maintain a degree of 3.

Lemma A.1. Any tree metric (a metric derived from a tree graph where the distance between two nodes is the length of the unique path connecting them) can be isometrically embedded into an ℓ_1 space [Bridson and Haefliger, 2013].

A.5 Tree-Based Wavelet

Wavelets [Mallat, 1999, Haar, 1911, Gavish et al., 2010] are powerful tools for signal and data analysis, combining the structural advantages of tree representations with the multi-resolution properties of wavelets. They organize data hierarchically, enabling efficient decomposition and reconstruction processes that adapt to the underlying signal’s structure. This adaptability makes them well-suited for tasks involving irregular or sparse data, where traditional grid-based wavelets may struggle. In these methods, the wavelet transform is guided by a tree structure, such as binary or quadtrees, which dictates how the data is partitioned and processed. The tree’s topology often reflects the inherent relationships within the data. This property allows tree-based wavelets to capture localized features and fine details while maintaining a global understanding of the data. Applications of wavelets span various fields, including image compression, denoising, and hierarchical data processing [Haar, 1911, Mallat, 1989, Daubechies, 1990]. Their

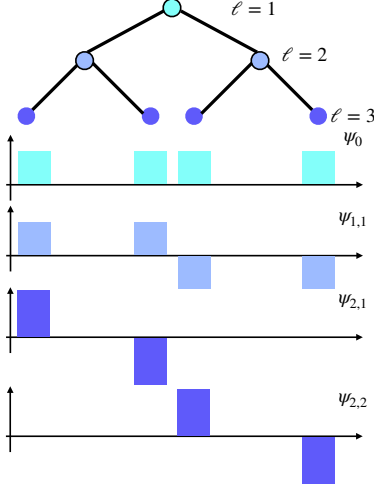


Figure 3: An illustration of a Haar basis induced by a binary tree.

efficiency and adaptability have also led to advancements in feature extraction and dimensionality reduction.

Consider a scalar function $f : \mathbf{X} \rightarrow \mathbb{R}$ defined on the data matrix. Let $S = \{f|f : \mathbf{X} \rightarrow \mathbb{R}\}$ be the space of all functions on the dataset. For the complete binary tree $\widehat{T}_c^{(1)}(\widehat{\mathbf{W}}_c^{(0)})$ with m leaves, let $\ell = 1, \dots, L_c$ denote the levels in the tree, where $\ell = 1$ is the root level and $\ell = L_c$ is the leaf level with m leaves. Define $\widetilde{\Upsilon}(\ell, \varepsilon)$ be the set of all leaves in the ε -th subtree of $\widehat{T}_c^{(1)}(\widehat{\mathbf{W}}_c^{(0)})$ at level ℓ . Define S^ℓ as the space of features that are constant across all subtrees at level ℓ , and let $\mathbf{1}_\mathbf{X}$ be a constant function on \mathbf{X} with the value 1. We have the following hierarchy

$$S^1 = \text{Span}(\mathbf{1}_\mathbf{X}), \quad S^{L_c} = S, \quad \text{and} \quad S^1 \subset \dots \subset S^{L_c}. \quad (12)$$

Therefore, the space S can be decomposed as

$$S = \left(\bigoplus_{\ell=1}^{L_c-1} Q^\ell \right) \bigoplus S^{L_c}, \quad (13)$$

where Q^ℓ is the orthogonal complement of S^ℓ . As the decoded tree $\widehat{T}_c^{(1)}(\widehat{\mathbf{W}}_c^{(0)})$ is a full binary tree, the Haar-like basis constructed from the tree is essentially the standard Haar basis [Haar, 1911], denoted by $\{\psi_{\ell, \varepsilon} \in \mathbb{R}^m\}$. At level ℓ , a subtree $\widehat{\Upsilon}_c(\ell, s)$ splits into two sub-subtrees $\widehat{\Upsilon}_c(\ell + 1, s_1)$ and $\widehat{\Upsilon}_c(\ell + 1, s_2)$. A zero-mean Haar wavelet $\psi_{\ell, s} \in \mathbb{R}^m$ has non-zero values only at the indices corresponding to leaves in the sub-subtrees and is piecewise constant on each of them. The set of these Haar wavelets, along with a constant vector ψ_0 , is complete and forms an orthonormal Haar basis. We collect all of these basis vectors as columns of matrix, denoted by $\Psi \in \mathbb{R}^{m \times m}$. Fig. 3 illustrates a Haar basis induced by a binary tree.

Proposition A.1 (Function Smoothness and Coefficient Decay [Gavish et al., 2010]). *Let $\psi_{\ell, \varepsilon}$ be the Haar basis function supported on $\widetilde{\Upsilon}(\ell, \varepsilon)$. If the function f is Lipschitz continuous, then for some $C > 0$,*

$$|\langle f, \psi_{\ell, \varepsilon} \rangle_S| \leq 4C d_{\widehat{T}_c^{(1)}(\widehat{\mathbf{W}}_c^{(0)})}(\widetilde{\Upsilon}(\ell, \varepsilon)), \quad (14)$$

where $d_{\widehat{T}_c^{(1)}(\widehat{\mathbf{W}}_c^{(0)})}(\widetilde{\Upsilon}(\ell, \varepsilon))$ is the tree distance between the internal node rooted at ε -subtree to the leaves.

Prop. A.1 indicates that the smoothness of the samples $\{\mathbf{X}_{i,:}\}$ leads to an exponential decay rate of their wavelet coefficients as a function of the tree level. Consequently, the wavelet coefficients can serve as a measure to assess the quality of the tree representation $\widehat{T}_c^{(1)}(\widehat{\mathbf{W}}_c^{(0)})$.

Proposition A.2 (L_1 Sparsity [Gavish et al., 2010]). *Consider a Haar basis ψ_Θ , where $\Theta \subset S$ and such that $|\psi_\Theta(j)| \leq 1/|\Theta|^{1/2}$. Let $f = \sum_\Theta \alpha_\Theta \psi_\Theta$ and assume $\sum_\Theta |\alpha_\Theta| \leq C$. For any $\kappa > 0$, the approximation $\tilde{f} = \sum_{|\Theta| < \kappa} \alpha_\Theta h_\Theta$,*

then

$$\|f - \tilde{f}\|_1 = \sum_{j \in [m]} |f(j) - \tilde{f}(j)| \leq C\sqrt{\kappa}. \quad (15)$$

Prop. A.2 implies that with L_1 approximation, it is sufficient to estimate the coefficients for function approximation. In the Haar domain, estimating these coefficients can be achieved using fast wavelet transform [Beylkin et al., 1991].

A.6 Wasserstein Distance

The Wasserstein Distance [Villani, 2009] measures the discrepancy between two probability distributions over a given metric space. It is related to optimal transport theory [Monge, 1781, Kantorovich, 1942], where the goal is to quantify the cost of transforming one distribution into another.

Consider two probability distributions μ and ν defined on a metric space (\mathcal{X}, d) , where d is the underlying metric. The p -Wasserstein distance, for $1 \leq p < \infty$, is defined as:

$$W_p(\mu, \nu) = \left(\inf_{\gamma \in \Gamma(\mu, \nu)} \int_{\mathcal{X} \times \mathcal{X}} d(x, y)^p d\gamma(x, y) \right)^{\frac{1}{p}}, \quad (16)$$

where $\Gamma(\mu, \nu)$ denotes the set of all joint probability measures on $\mathcal{X} \times \mathcal{X}$ with marginals μ and ν , i.e.,

$$\gamma(A \times \mathcal{X}) = \mu(A), \quad \gamma(\mathcal{X} \times B) = \nu(B), \quad (17)$$

for all measurable sets $A, B \subseteq \mathcal{X}$. For $p = 1$, the 1-Wasserstein distance simplifies to:

$$W_1(\mu, \nu) = \inf_{\gamma \in \Gamma(\mu, \nu)} \int_{\mathcal{X} \times \mathcal{X}} d(x, y) d\gamma(x, y), \quad (18)$$

which represents the minimal "cost" to transport the mass of μ to ν , which is also known as "earth mover's distance".

In the discrete setting, the Wasserstein Distance is commonly applied to two discrete probability distributions $\mu = \sum_{i=1}^n \mu_i \delta_{x_i}$ and $\nu = \sum_{j=1}^m \nu_j \delta_{y_j}$, where δ_x denotes the Dirac delta function at x , and $\mathbf{x} = \{x_i\}_{i=1}^n, \mathbf{y} = \{y_j\}_{j=1}^m$ are the support points of μ and ν , respectively. The distributions satisfy $\sum_{i=1}^n \mu_i = \sum_{j=1}^m \nu_j = 1$. In this case, the p -Wasserstein distance can be formulated as the solution to the following linear programming problem:

$$W_p(\mu, \nu)^p = \min_{\Gamma \in \Gamma(\mu, \nu)} \sum_{i=1}^n \sum_{j=1}^m d(x_i, y_j)^p \Gamma_{ij}, \quad (19)$$

where $\Gamma \in \mathbb{R}_{\geq 0}^{n \times m}$ is the transport matrix satisfying the marginal constraints:

$$\sum_{j=1}^m \Gamma_{ij} = \mu_i, \quad \sum_{i=1}^n \Gamma_{ij} = \nu_j, \quad \forall i, j. \quad (20)$$

When computing the Wasserstein distance between discrete probability distributions, the computational bottleneck often lies in constructing and processing the ground pairwise distance matrix. This matrix encodes the distances between every pair of discrete support points in the distributions, requiring $O(m^2)$ storage and $O(m^3 \log m)$ computation using traditional approaches [Peyré et al., 2019]. This complexity arises due to solving a linear program for the optimal transport problem, which scales poorly with the number of points m . Consequently, applying optimal transport directly becomes infeasible for large-scale datasets [Bonnel et al., 2011].

Several approximations have been proposed to reduce computational complexity. The Sinkhorn distance [Cuturi, 2013, Chizat et al., 2020] introduces an entropy regularization term to the objective function, enabling the use of iterative matrix scaling algorithms with computational complexity $O(m^2/\xi^2)$, where ξ is the regularization parameter. Graph-based methods exploit sparsity in the transport graph to simplify the problem structure, while sampling-based approaches approximate distributions using a subset of support points, reducing computational demand at the expense of accuracy.

A.7 Graph Convolutional Networks

Graph Convolutional Networks (GCNs) [Kipf and Welling, 2016] have gained significant attention in graph machine learning, where nodes in a graph are typically assumed in Euclidean spaces. By generalizing convolutional operations to graphs, GCNs effectively capture the graph relationships and dependencies between nodes. This capability enables high accuracy in tasks such as node classification, link prediction, and graph classification, making GCNs particularly valuable in applications like social networks [Hamilton et al., 2017], molecular structures [Duvenaud et al., 2015, Gilmer et al., 2017], knowledge graphs [Wang et al., 2019], recommendation systems [Ying et al., 2018], and drug discovery [Wu et al., 2018].

Consider a graph $G = (V, E, \mathbf{A})$ with a vertex set V containing n nodes, an edge set $E \subset V \times V$, an adjacency matrix $\mathbf{A} \in \mathbb{R}^{n \times n}$, and node features $\{\mathbf{x}_i \in \mathbb{R}^m\}_{i=1}^n$, where each \mathbf{x}_i consisting of m -dimensional node attribute. In each layer of general GCN message passing, the graph convolution can be divided into two steps: feature transformation and neighborhood aggregation. Specifically, the feature transform is defined by

$$\mathbf{h}_i^{(\ell)} = \mathbf{J}^{(\ell)} \mathbf{h}_i^{(\ell-1)}, \quad (21)$$

and the neighborhood aggregation is given by

$$\mathbf{h}_i^{(\ell)} = \sigma \left(\mathbf{h}_i^{(\ell)} + \sum_{s \in [[i]]} w_{is} \mathbf{h}_s^{(\ell)} \right), \quad (22)$$

where $\mathbf{h}_i^{(0)} = \mathbf{x}_i$ is the initial representation, $\mathbf{J}^{(\ell)}$ is the learnable weight matrix at the ℓ -layer, $\mathbf{h}_i^{(\ell-1)}$ is the i -th node representation at the $(\ell - 1)$ -th layer, $[[i]]$ is the set of the neighborhood nodes of the i -th node, w_{is} is the aggregation weight, and $\sigma(\cdot)$ is the non-linear activation function. Message passing is performed by stacking multiple graph convolutional layers that propagate messages over network neighborhoods. The feature transformation allows GCNs to learn meaningful representations, while the aggregation exploits graph structures.

A.8 Hyperbolic Graph Convolutional Networks

Hyperbolic Graph Convolutional Networks (HGNC) [Chami et al., 2019, Dai et al., 2021] extend GCN [Kipf and Welling, 2016] to hyperbolic geometry, utilizing its hierarchical representation ability to model graphs with latent hierarchical structures. By embedding nodes in hyperbolic space, HGNC achieves better representational capacity for hierarchical data while maintaining scalability. This adaptation introduces extended operations such as convolution and aggregation to respect the unique properties of hyperbolic geometry. HGNC has demonstrated its utility in various applications, including social network analysis, recommendation systems, and biological network modeling. It highlights the potential of integrating geometric insights into deep learning frameworks.

HGNCs adapt GCNs to hyperbolic geometry by embedding nodes in a hyperbolic space (e.g., Poincaré ball model and Lorentz model) and redefining graph convolution operations to respect hyperbolic properties. The following steps outline the construction of HGNCs.

Mapping the Node Features to Hyperbolic Representations. HGNC [Chami et al., 2019] first maps the input Euclidean features to the hyperboloid manifold via the exponential map at the origin by $\mathbf{x}_i^{H,(0)} = \text{Exp}_0([0, \mathbf{x}_i^\top]^\top)$, where the Exp is the exponential map given in App. A.1.

Hyperbolic Feature Transformation. The hyperbolic feature transformation utilizes the exponential and logarithmic maps to map points between hyperbolic and Euclidean spaces while applying Euclidean feature transformations. In particular, the linear transformation involves multiplying the embedding vector by a weight matrix and adding a bias term. Let $\mathbf{W} \in \mathbb{R}^{m' \times m}$ a weighted matrix, the hyperbolic matrix multiplication is defined by

$$\mathbf{W} \otimes \mathbf{x}_i^H = \text{Exp}_0(\mathbf{W}(\text{Log}_0(\mathbf{x}_i^H))). \quad (23)$$

The bias addition is defined by

$$\mathbf{x}_i^H \oplus \mathbf{b} = \text{Exp}_{\mathbf{x}_i^H}(\text{PT}_{0 \rightarrow \mathbf{x}_i^H}(\mathbf{b})), \quad (24)$$

where PT is the parallel transport given in App. A.1.

Hyperbolic Neighborhood Aggregation. The hyperbolic neighborhood aggregation is performed in tangent spaces with hyperbolic attention based on the hierarchical relation on the graph. Given the hyperbolic representations \mathbf{x}_i^H and \mathbf{x}_j^H , they are mapped to the tangent space at the origin. Attention weights w_{ij} are then computed using concatenation followed by a Euclidean Multi-Layer Perceptron (MLP). To aggregate node representations, the hyperbolic averaging method is proposed and given by

$$w_{ij} = \text{softmax}_{j \in [i]} (\text{MLP}(\text{Log}_0(\mathbf{x}_i^H) \parallel \text{Log}_0(\mathbf{x}_j^H))), \quad (25)$$

and

$$\text{AGG}(\mathbf{x}_i^H) = \text{Exp}_{\mathbf{x}_i^H} \left(\sum_{j \in [i]} w_{ij} \text{Log}_{\mathbf{x}_i^H}(\mathbf{x}_j^H) \right). \quad (26)$$

Then, a non-linear activation function is applied after the hyperbolic neighborhood aggregation.

B Additional Related Works

We discuss additional related works and their objectives.

Manifold Learning with the Wasserstein Distance. Manifold learning is a nonlinear dimensionality reduction technique for high-dimensional data that intrinsically lie on a manifold of lower dimension [Fefferman et al., 2016]. It allows for the integration of various geometric concepts into effective data analysis methods. Common manifold learning methods for deriving a manifold representation from discrete data samples typically involve constructing a graph where the data samples are associated with nodes, and edges are determined based on a notion of similarity. In many existing methods, the Euclidean norm is used to define these pairwise affinities. The utility of incorporating the Wasserstein distance in manifold learning [Gavish et al., 2010, Ankenman, 2014] has been demonstrated in numerous applications, including matrix organization [Mishne et al., 2017], neuronal pattern analysis [Mishne et al., 2016], and learning molecular shape spaces [Kileel et al., 2021]. In our work, we follow these works and, specifically, explore the diffusion operator [Coifman and Lafon, 2006] with the TWD matrix for coupled metric learning that respects the underlying hierarchical structures in both the samples and features.

Tree-Wasserstein Distances. The Tree-Wasserstein distance (TWD) is a computationally efficient variant of the Wasserstein distance, designed to compare probability distributions using a tree-based approximation of the ground metric. Its primary goal is to measure how much "mass" must be moved between distributions, with the movement cost guided by the structure of the tree. This tree structure simplifies computations by breaking the problem into smaller, more manageable components. By approximating the original metric with a tree metric, TWD simplifies the computation while retaining meaningful comparisons between distributions, as demonstrated in various studies [Indyk and Thaper, 2003, Le et al., 2019, Evans and Matsen, 2012, Yamada et al., 2022]. These methods typically provide an approximation of optimal transport (OT) in Euclidean spaces, enabling significant computational savings. For instance, the Quadtree method [Indyk and Thaper, 2003] recursively divides hypercubes to construct a random tree, which is then used to calculate the TWD. Flowtree [Backurs et al., 2020] refines this approach by focusing on optimal flow and its cost within the ground metric. Similarly, the Tree-Sliced Wasserstein Distance (TSWD) [Le et al., 2019] averages TWDs computed from randomly sampled trees, with variants such as TSWD-1, TSWD-5, and TSWD-10 depending on the number of sampled trees. Recent advancements include WQTWD and WCTWD [Yamada et al., 2022], which employ Quadtree or clustering-based tree structures and optimize tree weights to approximate the Wasserstein distance. UltraTree [Chen et al., 2024] introduces an ultrametric tree by minimizing OT regression cost, aiming to approximate the Wasserstein distance while respecting the original metric space.

Sliced-Wasserstein Distance. The Sliced-Wasserstein distance [Rabin et al., 2012, Bonneel et al., 2015] is a computationally efficient variant of the Wasserstein distance. Unlike the traditional Wasserstein distance, which involves solving a costly optimization problem in high dimensions, the Sliced-Wasserstein distance reduces complexity by projecting the distributions onto lower-dimensional subspaces, typically lines, and computing the Wasserstein distance in these projections. By averaging the results over many such slices, it provides a meaningful measure of

similarity while retaining much of the geometric structure inherent in the distributions. This approach is particularly advantageous in high-dimensional settings, where computational efficiency is critical, making it popular in applications such as generative modeling [Kolouri et al., 2019], domain adaptation [Bonet et al., 2023b], and statistical inference [Bonet et al., 2023a].

Unsupervised Ground Metric Learning. Ground metric learning aims to define a distance function that accurately reflects relationships between data points, playing a crucial role in tasks such as clustering, optimal transport, and dimensionality reduction. In many cases, labeled data is unavailable, making it necessary to develop unsupervised methods that rely solely on the structure and distribution of the data itself. Unsupervised ground metric learning focuses on using the inherent data distribution to learn a metric that captures meaningful pairwise relationships. This is achieved by optimizing a metric under assumptions such as preserving neighborhood structures, minimizing distortions in embeddings, or aligning with data-driven objectives like compactness or smoothness. These approaches avoid reliance on predefined metrics or external supervision, instead adapting to the specific properties of the dataset.

The interplay between feature relationships informed by sample relationships, and vice versa, has been used as a means in the ground metric learning [Huizing et al., 2022]. Specifically, considering the underlying manifold of samples and features has been extensively explored in various contexts. For instance, Ankenman [2014], Gavish and Coifman [2012], Gavish et al. [2010], Yair et al. [2017], Leeb and Coifman [2016] investigate this codependency for co-organization of data matrices, where the structure of features and samples is jointly analyzed to reveal meaningful patterns. Similarly, Mishne et al. [2016], Shahid et al. [2016], Mishne et al. [2019] extend this idea to dimensionality reduction by incorporating dependencies across both samples and features. These works often rely on the assumption of an underlying manifold structure to capture data organization.

C Proofs

We present the proofs supporting our theoretical analysis in Sec. 4. To aid in the proofs, we include several separately numbered propositions and lemmas.

Notation. Let $\mathcal{H}_m \subset \mathbb{R}_+^{m \times m}$ be a set of pairwise tree distance matrices for m points. That is, given $\mathbf{H} \in \mathcal{H}_m$, the following properties satisfy: (i) there is a weighted tree $T = (V, E, \mathbf{A})$ such that $\mathbf{H}(j, j') = d_T(j, j')$ for $j, j' \in [m]$, (ii) $\mathbf{H}(j, j) = 0$ for all $j \in [m]$, (iii) $\mathbf{H}(j_1, j_2) \leq \mathbf{H}(j_1, j_3) + \mathbf{H}(j_3, j_2)$ for $j_1, j_2, j_3 \in [m]$, and (v) $\mathbf{H}(j, j') = \mathbf{H}(j', j)$. Let $\mathcal{W}_{m \rightsquigarrow n} \subset \mathbb{R}_+^{n \times n}$ represent the set of pairwise OT distance matrices for n points, where the ground metric is given by the tree distance matrix $\mathbf{H} \in \mathcal{H}_m$ with m points. That is, given $\mathbf{B} \in \mathcal{W}_{m \rightsquigarrow n}$, the following properties satisfy: (i) $\mathbf{B}(i, i') = \text{OT}(\boldsymbol{\mu}_i, \boldsymbol{\mu}_{i'}, \mathbf{H}) = \text{TW}(\boldsymbol{\mu}_i, \boldsymbol{\mu}_{i'}, T)$ for any two probability distributions $\mathbf{x}_i, \mathbf{x}_{i'} \in \Delta_m$, (ii) $\mathbf{B}(i, i) = 0$ for all $i \in [n]$, (iii) $\mathbf{B}(i_1, i_2) \leq \mathbf{B}(i_1, i_3) + \mathbf{B}(i_3, i_2)$ for any probability distributions $\mathbf{x}_{i_1}, \mathbf{x}_{i_2}, \mathbf{x}_{i_3} \in \Delta_m$, and (v) $\mathbf{B}(i, i') = \mathbf{B}(i', i)$.

C.1 Proof of Theorem 1

Theorem 1. *The sequences $\mathbf{W}_r^{(l)}$ and $\mathbf{W}_c^{(l)}$ for $l \geq 1$ generated by CoHSL have at least one limit point, and all limit points are stationary points of Eq. (6) if $\gamma_r, \gamma_c > 0$.*

Proof. To prove convergence, we will show that the objective function $\mathcal{L}(\mathbf{W}_r, \mathbf{W}_c)$ in Eq. (2) satisfies the following conditions for convergence: (i) non-negative, (ii) monotonic decrease during iterative optimization, and (iii) lower bounded. First, each term in the objective function $\mathcal{L}(\mathbf{W}_r, \mathbf{W}_c)$ is a squared difference. Since squared terms are non-negative, the entire objective function is non-negative. Thus, the objective function is bounded below by 0, which provides a lower bound. Second, the optimization process alternates between updating \mathbf{W}_r and \mathbf{W}_c in such a way that each update step reduces the value of the objective function. Specifically, at each step, we update \mathbf{W}_r while holding \mathbf{W}_c fixed. The optimization problem for \mathbf{W}_r is a quadratic problem, and its solution decreases the objective function. That is, it guarantees a decrease in the objective function (or no change, in the worst case). Similarly, when \mathbf{W}_c is updated while keeping \mathbf{W}_r fixed, this is also a quadratic problem in \mathbf{W}_c , and solving it decreases the objective function. Since each update step (for \mathbf{W}_r and \mathbf{W}_c) reduces the value of $\mathcal{L}(\mathbf{W}_r, \mathbf{W}_c)$, the iterative process ensures a monotonic decrease in the objective function. Finally, since the objective function decreases monotonically with each

iteration and is bounded below, the iterative process converges to a local minimum by the descent lemma. Specifically, the iterative updates lead to a stationary point, which is a local minimum of the objective function.

In addition, we adapt the proof from [Huizing et al. \[2022\]](#), which can be summarized in two main parts. First, in each iteration, the Wasserstein distance between samples (or features) is used as the ground metric to compute the Wasserstein distance for the other dimension (features or samples), enabling unsupervised metric learning. Second, the proof relies on a continuous map from a locally contractible compact space onto itself, and by Brouwer's fixed-point theorem [[Brouwer, 1911](#)], such a map must have a fixed point.

Consider the set $\mathcal{S}_m = \{\mathbf{H}_c \in \mathcal{H}_m \mid \|\mathbf{H}_c\|_\infty \leq \theta_c \text{ and } \mathbf{H}_c(j, j') \geq \tilde{\theta}_c \forall j \neq j'\}$, the OT distance between samples with the ground metric \mathbf{H}_c is bounded by

$$\frac{\tilde{\theta}_c}{2} \|\mathbf{r}_i - \mathbf{r}_{i'}\|_1 \leq \text{OT}(\mathbf{r}_i, \mathbf{r}_{i'}, \mathbf{H}_c) \leq \frac{\theta_c}{2} \|\mathbf{r}_i - \mathbf{r}_{i'}\|_1,$$

where $\Delta_m \ni \mathbf{r}_i = \mathbf{X}_{i,:}^\top / \|\mathbf{X}_{i,:}\|_1$ as in [Sec. 4](#), and OT denotes the optimal transport distance between $\mathbf{r}_i, \mathbf{r}_{i'}$ given the ground metric \mathbf{H}_c . Similarly, consider $\mathcal{S}_n = \{\mathbf{H}_r \in \mathcal{H}_n \mid \|\mathbf{H}_r\|_\infty \leq \theta_r \text{ and } \mathbf{H}_r(i, i') \geq \tilde{\theta}_r \forall i \neq i'\}$, the OT distance between features using \mathbf{H}_r as the ground metric is bounded by

$$\frac{\tilde{\theta}_r}{2} \|\tilde{\mathbf{c}}_j - \mathbf{c}_{j'}\|_1 \leq \text{OT}(\tilde{\mathbf{c}}_j, \mathbf{c}_{j'}, \mathbf{H}_r) \leq \frac{\theta_r}{2} \|\tilde{\mathbf{c}}_j - \mathbf{c}_{j'}\|_1,$$

where $\Delta_n \ni \mathbf{c}_j = \mathbf{X}_{:,j} / \|\mathbf{X}_{:,j}\|_1$ as in [Sec. 4](#). Therefore, the refined TWDs in [Eq. \(6\)](#), where we consider the regularization function $\zeta(\cdot, \cdot)$, are respectively bounded by

$$\frac{\tilde{\theta}_c}{2} \|\mathbf{r}_i - \mathbf{r}_{i'}\|_1 + \gamma_c \zeta(\mathbf{r}_i, \mathbf{r}_{i'}) \leq \mathbf{W}_c(i, i') \leq \frac{\theta_c}{2} \|\mathbf{r}_i - \mathbf{r}_{i'}\|_1 + \gamma_c \zeta(\mathbf{r}_i, \mathbf{r}_{i'})$$

and

$$\frac{\tilde{\theta}_r}{2} \|\mathbf{c}_j - \mathbf{c}_{j'}\|_1 + \gamma_r \zeta(\mathbf{c}_j, \mathbf{c}_{j'}) \leq \mathbf{W}_r(j, j') \leq \frac{\theta_r}{2} \|\mathbf{c}_j - \mathbf{c}_{j'}\|_1 + \gamma_r \zeta(\mathbf{c}_j, \mathbf{c}_{j'}).$$

When constructing the pairwise tree distance matrices \mathbf{H}_r and \mathbf{H}_c using the embedding distance $d_{\mathcal{M}}$ in [Eq. \(11\)](#), we show that in [Prop. C.1](#) and [Lemma C.2](#), these distance matrices are bounded by the OT distance $\text{OT}(\cdot, \cdot, \mathbf{H}_r)$ and $\text{OT}(\cdot, \cdot, \mathbf{H}_c)$, i.e.,

$$\begin{aligned} \tilde{\varrho}_{\text{OT}(\cdot, \cdot, \mathbf{H}_r)} &\leq \mathbf{H}_c(j, j') \leq \varrho_{\text{OT}(\cdot, \cdot, \mathbf{H}_r)}, \\ \tilde{\varrho}_{\text{OT}(\cdot, \cdot, \mathbf{H}_c)} &\leq \mathbf{H}_r(i, i') \leq \varrho_{\text{OT}(\cdot, \cdot, \mathbf{H}_c)}, \end{aligned}$$

where $\varrho_{\text{OT}(\cdot, \cdot, \mathbf{H}_r)}$, $\tilde{\varrho}_{\text{OT}(\cdot, \cdot, \mathbf{H}_r)}$, $\varrho_{\text{OT}(\cdot, \cdot, \mathbf{H}_c)}$, and $\tilde{\varrho}_{\text{OT}(\cdot, \cdot, \mathbf{H}_c)}$ are defined in [Prop. C.1](#). Specifically, consider

$$\mathcal{P}_n = \{\mathbf{W}_c \in \mathcal{W}_{m \rightsquigarrow n} \mid \|\mathbf{W}_c\|_\infty \leq \varrho_{\text{OT}(\cdot, \cdot, \mathbf{H}_c)} \text{ and } \mathbf{W}_c(i, i') \geq \tilde{\varrho}_{\text{OT}(\cdot, \cdot, \mathbf{H}_c)} \forall i \neq i'\},$$

and

$$\mathcal{P}_m = \{\mathbf{W}_r \in \mathcal{W}_{n \rightsquigarrow m} \mid \|\mathbf{W}_r\|_\infty \leq \varrho_{\text{OT}(\cdot, \cdot, \mathbf{H}_r)} \text{ and } \mathbf{W}_r(i, i') \geq \tilde{\varrho}_{\text{OT}(\cdot, \cdot, \mathbf{H}_r)} \forall i \neq i'\}.$$

The function

$$(\mathbf{W}'_r, \mathbf{W}'_c) \mapsto (\Phi_{\mathbf{W}_c}(\mathbf{C}), \mathbf{W}_c = \Phi_{\mathbf{W}_r}(\mathbf{R}))$$

in [Alg. 1](#) is a two-fold continuous and contraction map

$$((\mathcal{S}_n \times \mathcal{S}_m) \times (\mathcal{P}_n \times \mathcal{P}_m)) \rightarrow ((\mathcal{S}_n \times \mathcal{S}_m) \times (\mathcal{P}_n \times \mathcal{P}_m))$$

that are locally contractible compact sets. Therefore, based on the topological properties in Brouwer's fixed-point theorem [[Brouwer, 1911](#)], [Eq. \(6\)](#) has at least one limit point, and all these limit points correspond to a fixed point. \square

Proposition C.1. Let $\|\cdot\|_{\mathcal{R}}$ be a norm in \mathbb{R}^m . Let $\mathcal{X} = \{\mathbf{x}_i\}_{i=1}^n$ be a set of data points in an ambient space \mathbb{R}^m . If the diffusion operator is constructed by a Gaussian kernel with the norm $\|\cdot\|_{\mathcal{R}}$, then for all $i \neq i'$, the embedding distance $d_{\mathcal{M}}$ can be bounded by

$$\tilde{\varrho}_{\mathcal{R}} \leq d_{\mathcal{M}}(i, i') \leq \varrho_{\mathcal{R}}, \quad (27)$$

where $\varrho_{\mathcal{R}}, \tilde{\varrho}_{\mathcal{R}} \in \mathbb{R}_{>0}$ are constants controlled by $\|\cdot\|_{\mathcal{R}}$.

Proof. Let $c_{\mathcal{R}}$ and $C_{\mathcal{R}}$ be the bounds of the norm $\|\cdot\|_{\mathcal{R}}$ for any two data points $\mathbf{x}_i, \mathbf{x}_{i'} \in \mathcal{X}$, that is, $c_{\mathcal{R}} \leq \|\cdot\|_{\mathcal{R}}^2 \leq C_{\mathcal{R}}$. The pairwise affinity matrix is constructed by $\mathbf{K}(i, i') = \exp(-\|\mathbf{x}_i - \mathbf{x}_{i'}\|_{\mathcal{R}}^2 / \epsilon)$, and it is bounded by $\exp(-C_{\mathcal{R}}/\epsilon) \leq \mathbf{K}(i, i') \leq \exp(-c_{\mathcal{R}}/\epsilon)$. Therefore, the diffusion operator is bounded by

$$\frac{1}{n} \frac{\exp(-C_{\mathcal{R}}/\epsilon)}{\exp(-c_{\mathcal{R}}/\epsilon)} \leq \mathbf{P}(i, i') \leq \frac{1}{n} \frac{\exp(-c_{\mathcal{R}}/\epsilon)}{\exp(-C_{\mathcal{R}}/\epsilon)}.$$

This implies that $\frac{1}{B_{\mathcal{R}}} \leq \|\mathbf{P}\|_{\infty} \leq B_{\mathcal{R}}$, where $1 < B_{\mathcal{R}} = \frac{\exp(-c_{\mathcal{R}}/\epsilon)}{\exp(-C_{\mathcal{R}}/\epsilon)}$. Since the matrix \mathbf{P} is non-negative [Seneta, 2006, Horn and Johnson, 2012], we have

$$\frac{1}{n} \left(\frac{1}{B_{\mathcal{R}}} \right)^t \leq \mathbf{P}^t(i, i') \leq \frac{1}{n} B_{\mathcal{R}}^t.$$

In addition, we can upper bound the Hellinger measure and the ℓ_1 norm of the diffusion operator respectively by

$$\left\| \sqrt{\mathbf{P}^t(i, :)} - \sqrt{\mathbf{P}^t(i', :)} \right\|_2 \leq B_{\mathcal{R}}^{\frac{t}{2}} - \left(\frac{1}{B_{\mathcal{R}}} \right)^{\frac{t}{2}} \quad \text{and} \quad \left\| \mathbf{P}^t(i, :) - \mathbf{P}^t(i', :) \right\|_1 \leq B_{\mathcal{R}}^t - \left(\frac{1}{B_{\mathcal{R}}} \right)^t.$$

Then, the embedding distance can be bounded by a function $\varrho_{\mathcal{R}}$ that is dependent on the norm $\|\cdot\|_{\mathcal{R}}$ in the ambient space. Specifically, the upper bound $\varrho_{\mathcal{R}}$ is given by

$$\begin{aligned} & d_{\mathcal{M}}(i, i') \\ &= \sum_{k=0}^K 2 \sinh^{-1} \left(2^{-k/2+1} \left\| \sqrt{\mathbf{P}^{2^{-k}}(i, :)} - \sqrt{\mathbf{P}^{2^{-k}}(i', :)} \right\|_2 \right) \\ &\leq \sum_{k=0}^K 2 \sinh^{-1} \left(2^{-k/2+1} \left(B_{\mathcal{R}}^{\frac{2^{-k}}{2}} - \left(\frac{1}{B_{\mathcal{R}}} \right)^{\frac{2^{-k}}{2}} \right) \right) \\ &\leq \sum_{k=0}^K \left(2^{-k/2+1} \left(B_{\mathcal{R}}^{\frac{2^{-k}}{2}} - \left(\frac{1}{B_{\mathcal{R}}} \right)^{\frac{2^{-k}}{2}} \right) \right) \\ &= \varrho_{\mathcal{R}}. \end{aligned}$$

On the other hand, the lower bound can be expressed by

$$\begin{aligned} & d_{\mathcal{M}}(i, i') = \\ &= \sum_{k=0}^K 2 \sinh^{-1} \left(2^{-k/2+1} \left\| \sqrt{\mathbf{P}^{2^{-k}}(i, :)} - \sqrt{\mathbf{P}^{2^{-k}}(i', :)} \right\|_2 \right) \\ &\stackrel{(1)}{\geq} \sum_{k=0}^K 2^{-k/2} \left\| \mathbf{P}^{2^{-k}}(i, :) - \mathbf{P}^{2^{-k}}(i', :) \right\|_1 \\ &\stackrel{(2)}{\geq} \epsilon_{\mathcal{R}} \sum_{k=0}^K 2^{-k/2} \\ &= \tilde{\varrho}_{\mathcal{R}}, \end{aligned}$$

where transition (1) is based on Lemma C.1, and transition (2) is based on Lemma 3 in Leeb and Coifman [2016]. \square

Lemma C.1. Let p, q be two probability distributions on \mathcal{X} . For a constant $k \in \mathbb{Z}_{\geq 0}$, we have

$$2 \sinh^{-1} \left(2^{-k/2+1} \|\sqrt{p} - \sqrt{q}\|_2 \right) \geq 2^{-k/2} \|p - q\|_1, \quad (28)$$

where $\|\sqrt{p} - \sqrt{q}\|_2$ is the unnormalized Hellinger distance between p and q .

Lemma C.2. Let $\|\cdot\|_{\mathcal{R}}$ be a norm in \mathbb{R}^m . Let $\mathcal{X} = \{\mathbf{x}_i\}_{i=1}^n$ be a set of data points in an ambient space \mathbb{R}^m . The tree metric obtained by the hyperbolic tree decoding in Alg. 3 can be bounded by

$$\tilde{\varrho}_{\mathcal{R}} \leq d_B(i, i') \leq \varrho_{\mathcal{R}}, \quad (29)$$

where $\varrho_{\mathcal{R}}, \tilde{\varrho}_{\mathcal{R}} \in \mathbb{R}_{>0}$ are constants controlled by $\|\cdot\|_{\mathcal{R}}$.

Proof. By Thm. A.1 and Thm. A.2, we note that the decoded tree metric, the tree metric, and the embedding distance are bilipschitz equivalent, i.e., $d_B \simeq d_T \simeq d_{\mathcal{M}}$. Applying Prop. C.1, we can show that the decoded tree metric d_B is bounded by $\tilde{\varrho}_{\mathcal{R}} \leq d_B(i, i') \leq \varrho_{\mathcal{R}}$, where $\|\cdot\|_{\mathcal{R}}$ is the norm used in constructing the Gaussian kernel for the diffusion operator employed in hyperbolic diffusion tree decoding in Alg. 3. \square

C.2 Proof of Theorem 2

Theorem 2 The sequences $\widehat{\mathbf{W}}_r^{(l)}$ and $\widehat{\mathbf{W}}_c^{(l)}$ for $l \geq 1$ generated by CoHSL-Wavelet have at least one limit point, and all limit points are stationary points of Eq. (8) if $\gamma_r, \gamma_c > 0$.

Proof. Note that when the Haar filters $\varphi_{\widehat{\mathbf{W}}_r^{(l)}}(\mathbf{X}^{(l)})$ and $\varphi_{\widehat{\mathbf{W}}_c^{(l)}}(\mathbf{Z}^{(l)})$ are applied to samples and features, the resulting outputs remain bounded. This is because the filters operate on a subset of the Haar representation of the original data. Furthermore, since Haar wavelets are linear and bounded operators, updating the data with these wavelet filters preserves the convexity of the objective function. In addition, the wavelet transform and filtering are stable and invertible (e.g., using soft-thresholding). The bounded nature of these filters further aids convergence by regularizing the problem and mitigating extreme updates. The proof in Theorem 1 relies on a two-fold continuous and contraction mapping. Incorporating bounded wavelets introduces an additional continuous and contraction mapping, keeping the iterative process within locally contractible and compact sets. As a result, based on the topological properties of Brouwer’s fixed-point theorem [Brouwer, 1911], similar to Thm. 1, Eq. (8) has at least one limit point, with all such points corresponding to fixed points. \square

D Additional Details on Experimental Study

We provide a detailed description of the experimental setups and additional specifics in Sec. 6. The experiments are conducted on NVIDIA DGX A100.

D.1 Datasets

We evaluate our methods on word-document data, scRNA-seq data, and hierarchical graph data. We report the details of the dataset statistics in Tab. 4.

Word-document benchmarks. We consider four word-document benchmarks in Kusner et al. [2015]: (i) the BBCSPORT dataset, consisting of 13,243 bags of words (BOW) and 517 articles categorized into five sports types, (ii) the TWITTER dataset, comprising 6,344 BOW and 2,176 tweets classified into three types of sentiment, (iii) the CLASSIC dataset, including 24,277 BOW and 4,965 academic papers from four publishers, and (iv) the AMAZON dataset, containing 42,063 BOW and 5,600 reviews of four products. We used the pre-trained Word2Vec embeddings¹ [Mikolov et al., 2013] as the word embedding vector, trained on the Google News dataset, which includes approximately 3 million words and phrases. Word2Vec represents these words and phrases as vectors in \mathbb{R}^{300} . The document types serve as labels for classification tasks.

¹<https://code.google.com/p/word2vec>

Dataset	# Samples / Nodes	# Classes	# Edges	# Features
BBCSPORT	517	5	-	13,243 BOW
TWITTER	2,176	3	-	6,344 BOW
CLASSIC	4,965	4	-	24,277 BOW
AMAZON	5,600	4	-	42,063 BOW
ZEISEL	3,005	47	-	4,000 Genes
CBMC	8,617	56	-	500 Genes
DISEASE	1,044	2	1,043	1,000
AIRPORT	3,188	4	18,631	4
PUBMED	19,717	3	88,651	500
CORA	2,708	7	5,429	1,433

Table 4: Summary of dataset statistics for word-document, scRNA-seq, and hierarchical graph datasets.

Single Cell RNA Sequencing Data. For scRNA-seq data, we analyze two scRNA-seq datasets from [Dumitrascu et al. \[2021\]](#): (i) the ZEISEL dataset: From the mouse cortex and hippocampus [[Zeisel et al., 2015](#)], comprising 4,000 gene markers and 3,005 single cells, and (ii) the CBMC dataset: from a cord blood mononuclear cell study [[Stoeckius et al., 2017](#)], consisting of 500 gene markers and 8,617 single cells. We used the divisive biclustering method in [Zeisel et al. \[2015\]](#) to obtain 47 classes for Zeisel and 56 classes for the CBMC. We use Gene2Vec as the word embedding vectors. For these datasets, cell types are used as labels in cell classification tasks.

Hierarchical Graphs. For hierarchical graph data, we consider the following datasets: (i) the DISEASE dataset: constructed by simulating the SIR disease spreading model [[Anderson and May, 1991](#)], where node labels indicate infection status and node features indicate susceptibility to the disease [[Chami et al., 2019](#)], (ii) the AIRPORT dataset: a flight network dataset where nodes represent airports and edges represent airline routes. The label of a node indicates the population of the country where the airport is located [[Chami et al., 2019](#)], (iii) the CORA dataset: a citation network containing 2,708 nodes, 5,429 edges, and 1,433 features per node, with papers classified into seven machine learning categories [[Sen et al., 2008](#)], and (iv) the PUBMED dataset: Another citation network with 19,717 nodes, 44,338 edges, and 500 features per node, encompassing three classes of medicine publications [[Sen et al., 2008](#)].

D.2 Initial Distance Metric and Scales

In the step of constructing the hyperbolic diffusion tree, the Gaussian kernel scale is set to $\{0.1, 1, 2, 5, 10\} \times \chi$, where χ represents the median of the pairwise distances. The number of hyperbolic spaces in the product manifold is determined by $K \in \{0, \dots, 19\}$. Since these parameters are highly task-dependent and there is no universal choice that works for all cases, we employ Optuna [[Akiba et al., 2019](#)] to systematically explore the parameter space and efficiently identify the optimal settings for each specific task. We compute the initial distance matrices $\mathbf{M}_c \in \mathbb{R}^{m \times m}$ (between features) and $\mathbf{M}_r \in \mathbb{R}^{n \times n}$ (between samples) based on cosine similarity computed in the ambient space for both word-document data and scRNA-seq data, following previous work [[Jaskowiak et al., 2014](#), [Kenter and De Rijke, 2015](#)]. In practice, as noted in Sec. 4, we observe that when γ_r and γ_c are sufficiently large, the canonical TWDs from Alg. 1 and Alg. 2 converge to unique solutions. It is important to note that such property may not exist when using other tree construction or TWD methods. This differs from existing TWDs and manifold learning techniques, where the initial distance metric significantly influences their effectiveness. Notably, we observe that among various metrics—random distance, Euclidean distance, and cosine similarity—using cosine similarity as the initial distance metric leads to faster convergence for both word-document and scRNA-seq data, as demonstrated in App. E. For hierarchical graph data, we use the hierarchical distance between nodes (i.e., samples) as the initialization distance $\mathbf{M}_r \in \mathbb{R}^{n \times n}$ (as a prior) and the distance based on cosine similarity as the initial distance between node attributes (i.e., features). We observe in App. E that using the hierarchical distance between samples leads to faster convergence. We optimize all the hyperparameters using Optuna [[Akiba et al., 2019](#)].

D.3 Scaling to Large Datasets

In our iterative optimization process, one key step in hyperbolic diffusion tree decoding involves constructing diffusion operators [Coifman and Lafon, 2006] between both samples and features. Although applying eigendecomposition to the diffusion operator can be computationally intensive, recent developments in diffusion geometry have introduced various techniques to significantly reduce the runtime and space complexity of this process. In particular, our work focuses on the diffusion landmark approach [Shen and Wu, 2022], which enhances scalability by reducing the complexity from $O(n^3)$ to $O(n^{1+2\beta})$ for samples and from $O(m^3)$ to $O(m^{1+2\beta})$ for features, where $\beta < 1$ represents the proportional size of the landmark set relative to the original dataset. We briefly describe the diffusion landmark approach below for the setup for samples and note that it can be seamlessly applied to features. For more details, refer to [Shen and Wu, 2022].

Given a set of samples $\mathcal{X} = \{\mathbf{x}_i\}_{i=1}^n \subseteq \mathbb{R}^m$ in an ambient space \mathbb{R}^m , let $\mathcal{X}' = \{\mathbf{x}'_i\}_{i=1}^{n'} \subset \mathcal{X} \subseteq \mathbb{R}^m$ be the landmark set of \mathcal{A} , where $\beta = \log_n(n') < 1$. The affinity matrix between the landmark set \mathcal{X}' and the original set \mathcal{X} is denoted by $\widehat{\mathbf{K}} = \exp(-\widehat{\mathbf{M}}^{\circ 2}/\epsilon)$, where $\widehat{\mathbf{M}}(i, i')$ represents a suitable distance between the sample $\mathbf{x}_i \in \mathcal{X}$ and the sample $\mathbf{x}'_{i'} \in \mathcal{X}'$, and $\epsilon > 0$ is the scale parameter. Let $\widehat{\mathbf{D}}$ be a diagonal matrix, where $\widehat{\mathbf{D}}(i, i) = \delta_i^\top \widehat{\mathbf{K}} \widehat{\mathbf{K}}^\top \mathbf{1}_n$ and $\mathbf{1}_n = [1, \dots, 1] \in \mathbb{R}^n$. The landmark-affinity matrix $\widehat{\mathbf{Y}} = \widehat{\mathbf{K}} \widehat{\mathbf{K}}^\top \in \mathbb{R}^{n \times n}$ has an eigen-structure similar to the diffusion operator, which can be computed by applying SVD to the matrix $\widehat{\mathbf{D}}^{-1/2} \widehat{\mathbf{K}} = \widehat{\mathbf{U}} \widehat{\mathbf{\Lambda}} \widehat{\mathbf{V}}$. To construct the diffusion operator on \mathcal{X} , one can use the landmark set \mathcal{X}' and their eigenvectors. These eigenvectors can be directly used to construct the hyperbolic diffusion tree between samples, enabling the analysis of datasets larger than ten thousand data points, e.g., word-document data, scRNA-seq data, and hierarchical graph data, as shown in Sec. 6.

D.4 Document and Cell Classification Setup

To assess the performance of our approaches in unsupervised Wasserstein distance learning, we conduct evaluations on document and cell classification. The datasets are split into 70% training set and 30% testing set, in line with previous studies [Kusner et al., 2015, Huang et al., 2016]. Both the underlying sample tree and feature tree learning, as well as the kNN model, are subjected to this random split. The trees constructed from the training data can be reused to process new data. In each run, we employ a k NN classifier with k values from the set $\{1, 3, 5, 7, 9, 11, 13, 15, 17, 19\}$, following Kusner et al. [2015], Huang et al. [2016]. The random split is performed five times, and we report the best average classification accuracy over these five runs.

D.5 Incorporating CoHSL with HGCN

In CoHSL, we assume that the hierarchical data exhibits latent hierarchical structures in both samples and features. However, this assumption can be extended to a broader context. Specifically, our methods are applicable to coupled hierarchical data where one mode of the hierarchical structures is known in advance and can be used for initialization. Through iterative refinement, our method can extract intrinsic relationships, where the hierarchical structure between the samples is informed by the relationships between the features, and vice versa. We demonstrate a broad application of this approach by integrating it into hyperbolic graph convolution. Hyperbolic geometry has gained traction in recent research due to its ability to capture hierarchical data effectively [Nickel and Kiela, 2017, 2018]. Recent studies have proposed developing Graph Convolutional Networks (GCNs) in hyperbolic spaces [Chami et al., 2019, Liu et al., 2019, Dai et al., 2021, Zhang et al., 2021], where node features are projected from Euclidean space to hyperbolic space based on the hierarchical structure of samples. In this context, node features are projected according to the hierarchical structures of the samples. We demonstrate that CoHSL and CoHSL-Wavelet can be seamlessly incorporated as preprocessing steps in hyperbolic graph convolutional networks (HGCNs) [Chami et al., 2019, Dai et al., 2021]. We first demonstrate the multi-scale hyperbolic embedding as a node representation derived from the data as the input node features. We then illustrate the process of performing hyperbolic feature transformation and hyperbolic neighborhood aggregation. The CoHSL-Wavelet HGCN follows a similar development, with the hyperbolic node representation based on Alg 2.

Hyperbolic Feature Transformation. Note that in addition to the coupled TWDs \mathbf{W}_r and \mathbf{W}_c , the hyperbolic tree decoding is based on a multi-scale hyperbolic embedding (as described in Sec. 3), which can be used as the hyperbolic representation. The multi-scale hyperbolic embedding for the i -th node, denoted as $[\mathbf{y}_i^0, \dots, \mathbf{y}_i^K]$, is a

point in a product manifold of Poincaré half-space [Lin et al., 2023]. Therefore, this representation can be viewed as a hyperbolic transformation of the Euclidean node features.

The Poincaré half-space is advantageous for representing the exponentially increasing scale of diffusions in hyperbolic space [Lin et al., 2023]. However, due to the simpler computation of Riemannian operations in the Lorentz model \mathbb{L}^{n+1} and the equivalence between the two models [Ratcliffe et al., 1994], the Lorentz model is used for feature transformation, following Chami et al. [2019], Dai et al. [2021]. The hyperbolic feature transformation is performed by first transforming points from the Poincaré half-space to the Lorentz model, followed by applying the Lorentz linear transformation [Dai et al., 2021] and mapping back to Poincaré half-space. Second, since the hyperbolic feature transformation is manifold-preserving, we propose hyperbolic aggregation as the weighted Riemannian mean of the neighborhood points, followed by a non-linear activation function.

The Poincaré half-space offers a natural representation of how scales increase exponentially in hyperbolic spaces [Lin et al., 2023]. Despite this, performing Riemannian operations is more straightforward in the Lorentz model [Nickel and Kiela, 2018, Chami et al., 2019]. Due to the equivalence between the Poincaré half-space and the Lorentz model, we utilize a diffeomorphism Lin et al. [2024b] to map points from the Poincaré half-space to the Lorentz model by

$$\widehat{\mathbf{y}}_i^k = \mathcal{P}(\mathbf{y}_i^k) = \frac{(1 + \|\widetilde{\mathbf{y}}_i^k\|^2, 2\widetilde{\mathbf{y}}_i^k(1), \dots, 2\widetilde{\mathbf{y}}_i^k(n+1))}{1 - \|\widetilde{\mathbf{y}}_i^k\|^2}, \quad (30)$$

where

$$\widetilde{\mathbf{y}}_i^k = \frac{(2\mathbf{y}_i^k(1), \dots, 2\mathbf{y}_i^k(n), \|\mathbf{y}_i^k\|^2 - 1)}{\|\mathbf{y}_i^k\|^2 + 2\mathbf{y}_i^k(n+1) + 1}.$$

The feature transformation is essentially a linear transformation defined by a matrix-vector multiplication. The hyperbolic feature transformation involves transforming points from the Poincaré half-space to the Lorentz model using Eq. (9). Subsequently, the Lorentz linear transformation [Dai et al., 2021] is applied

$$\mathbf{h}_i^k = \mathbf{J}\widehat{\mathbf{y}}_i^k \text{ s.t. } \mathbf{J} = \begin{bmatrix} 1, & \mathbf{0}^\top \\ \mathbf{0}, & \widetilde{\mathbf{J}} \end{bmatrix} \text{ and } \widetilde{\mathbf{J}}^\top \widetilde{\mathbf{J}} = \mathbf{I}. \quad (31)$$

The Lorentz linear transformation is used as the hyperbolic feature transformation. Finally, the points are mapped back to the Poincaré half-space.

Hyperbolic Neighborhood Aggregation. As the hyperbolic feature transformation preserves the manifold structure, once the points are mapped back to the Poincaré half-space, the hyperbolic neighborhood aggregation is defined as follows

$$\widehat{\mathbf{h}}_i^{(\ell),k} = \sigma \left(\sum_{s \in [[i]]} (w_{is} \mathbf{h}_s^{(\ell),k}) \right), \quad (32)$$

where σ is a non-linear activation function. Unlike the Lorentz model described in Chami et al. [2019], Dai et al. [2021], the non-linear activation function in the Poincaré half-space does not violate the manifold constraints. This means that non-linear activation in the Poincaré half-space is manifold-preserving. Additionally, the point assigned to the non-linear activation function can be interpreted as a weighted Riemannian mean in the Poincaré half-space. It is important to note that our hyperbolic feature transformation and neighborhood aggregation are similar to the methods in Dai et al. [2021], where these operations are performed directly on the manifold. This approach differs from Chami et al. [2019], where points are projected from the manifold to the tangent space and back. The non-linear activation function is then applied to the hyperbolic representation.

Hierarchical Graph Data Splits and Evaluation. For link prediction tasks, we divide the edges into 85% for training, 5% for validation, and 10% for testing. For node classification, the splits vary by dataset: 70%/15%/15% for AIRPORT, 30%/10%/60% for DISEASE, and the standard setup of 20 training examples per class for CORA and PUBMED. These configurations align with established practices in prior studies [Chami et al., 2019, Dai et al., 2021]. We evaluate link prediction using ROC AUC, the DISEASE dataset with the F1 score, and node classification tasks on the AIRPORT, PUBMED, and CORA datasets using accuracy.

	Word-Document Data				scRNA-seq Data	
	BBCSPORT	TWITTER	CLASSIC	AMAZON	ZEISEL	CBMC
Quadtree	95.5±0.5	69.6±0.8	95.9±0.4	89.3±0.3	80.1±1.2	80.6±0.6
Flowtree	95.3±1.1	70.2±0.9	94.4±0.6	90.1±0.3	81.7±0.9	81.8±0.9
WCTWD	92.6±2.1	69.1±2.6	93.7±2.9	88.2±1.4	81.3±4.9	78.4±3.3
WQTWD	94.3±1.7	69.4±2.4	94.6±3.2	87.4±1.8	80.9±3.5	79.1±3.0
UltraTree	93.1±1.5	68.1±3.2	92.3±1.9	86.2±3.1	83.9±1.6	82.3±2.6
TSWD-1	87.6±1.9	69.8±1.3	94.5±0.5	85.5±0.6	79.6±1.8	72.6±1.8
TSWD-5	88.1±1.3	70.5±1.1	95.9±0.4	90.8±0.1	81.3±1.4	74.9±1.1
TSWD-10	88.6±0.9	70.7±1.3	95.9±0.6	91.1±0.5	83.2±0.8	76.5±0.7
SWCTWD	92.8±1.2	70.2±1.2	94.1±1.8	90.2±1.2	81.9±3.1	78.3±1.7
SWQTWD	94.5±1.0	70.6±1.9	95.4±2.0	89.8±1.1	80.7±2.5	79.8±2.5
MST-TWD	88.4±1.9	68.2±1.9	90.0±3.1	86.4±1.2	80.1±3.1	76.2±2.5
TR-TWD	89.2±0.9	70.2±0.7	92.9±0.8	88.7±1.1	80.3±0.7	78.4±1.2
HHC-TWD	85.3±1.8	70.4±0.4	93.4±0.8	88.5±0.7	82.3±0.7	77.3±1.1
gHHC-TWD	83.2±2.4	69.9±1.8	90.3±2.2	86.9±2.0	79.4±1.9	73.6±1.6
UltraFit-TWD	84.9±1.4	69.5±1.2	91.6±0.9	87.4±1.6	81.9±3.3	77.8±1.2
WMD	95.4±0.7	71.3±0.6	97.2±0.1	92.6±0.3	-	-
GMD	-	-	-	-	84.2±0.7	81.4±0.7
HD-TWD	96.1±0.4	73.4±0.2	96.9±0.2	93.1±0.4	89.1±0.4	84.3±0.3

Table 5: Document and cell classification accuracy of initial TWD (without iterative refinement).

E Additional Experimental Results

E.1 Ablation Study

To demonstrate that our iterative procedure effectively improves the coupled hierarchical structure learning for both samples and features, we begin by presenting the initial TWD and OT baselines, which exclude the iterative updates between samples and features. Tab. 5, taken from Lin et al. [2024a], shows the document and cell classification accuracy using the initial Wasserstein distance. Compared to Tab. 2, the results indicate that the iterative scheme improves most Wasserstein distance, indicating that the proposed iterative procedure enhances the distance metric learning methods.

E.2 Sparse Approximation

In Tab. 1, the L_1 norm of the Haar coefficients is presented. For our methods, the values are reported after convergence, whereas for competing methods, we report the values either at convergence or, if convergence is not reached, after 25 iterations. Fig. 4 illustrates the evolution of the L_1 norm of the Haar coefficients over iterations for all methods. Our methods demonstrate a consistent reduction in the L_1 norm, reaching convergence. This reduction is a byproduct of our approach to learning a coupled hierarchical representation of the data, rather than the explicit objective of the CoHSL algorithm. The competing methods show some improvement, but it is inconsistent across iterations. While a few achieve convergence, the final L_1 norm remains higher compared to our methods.

E.3 Empirical Convergence

We report the classification accuracy at each iteration for CoHSL, CoHSL-Wavelet, and the baseline methods Co-TWDs and Co-OTs. Fig. 5 shows the results for both scRNA-seq and word-document datasets. For scRNA-seq datasets, we compare against the gene-based Co-OT using GMD as the baseline, while for word-document datasets, we use Co-WMD as the baseline. We see that the CoHSL improves the classification accuracy of TWDs (i.e., the TWDs reported in Tab. 5, the first half iteration in Alg. 1) in both scRNA-seq and word-document datasets as reported in Tab. 2. In addition, the proposed CoHSL outperforms the competing Co-TWD and Co-OTs baselines by a large margin in scRNA-seq and word-document datasets over the iterations. We note that the classification accuracy of the

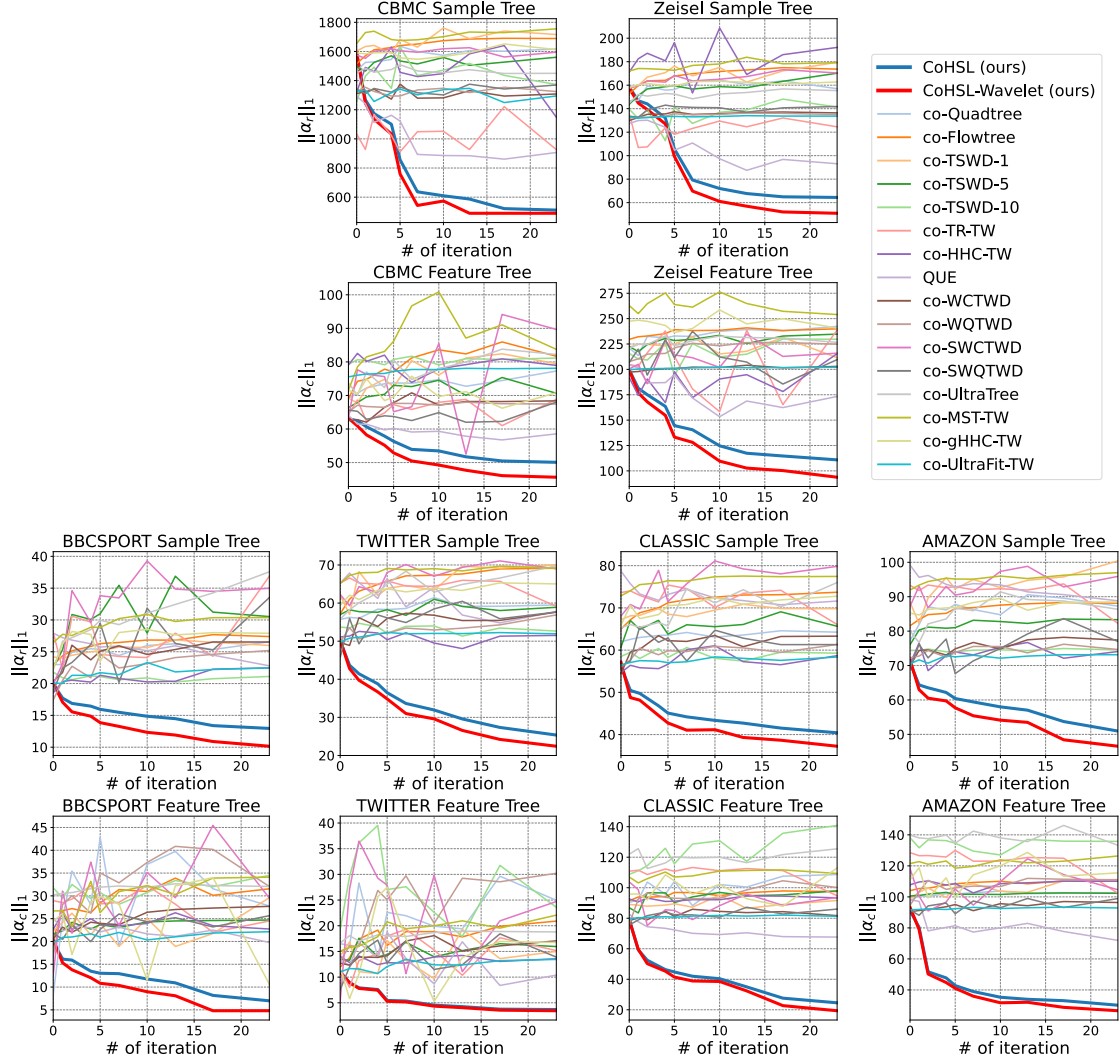


Figure 4: Coefficient decay in the sparse approximation of samples and features over the iterative processes.

competing Co-TWDs and Co-OTs (e.g., Co-Flowtree, Co-GMD, and Co-WMD) is also improved from their TWD and OT distances in Tab. 2, showing the optimization technique in Alg. 1 employed in the baselines also captures the coupling between rows and columns that further reveals the intrinsic Wasserstein metrics. We note that such empirical improvements were not shown in Co-Quadtree, Co-TSWD, Co-TR-TW, and Co-HHC-TW in every classification task. Notably, we observe that the classification performance of CoHSL converges in a few iterations, empirically supporting our theoretical claim in Thm. 1. We see that QUE and WSV also reach empirical convergence, however, their classification performances are less effective than our CoHSL. We remark that the Co-Quadtree, Co-TSWD, Co-TR-TW, and Co-HHC-TW do not have such experimental convergences due to the random sampling of the trees and random initialization in tree constructions.

E.4 Runtime Analysis

Fig. 6 compares the runtime of our methods with co-TWDs and co-OTs. While our methods are marginally slower than co-TSWD-1 and co-TR-TWD, they offer substantial improvements in classification accuracy, as highlighted in Tab. 2. This trade-off reflects the strength of our approach in achieving better classification performance while maintaining competitive runtime efficiency.

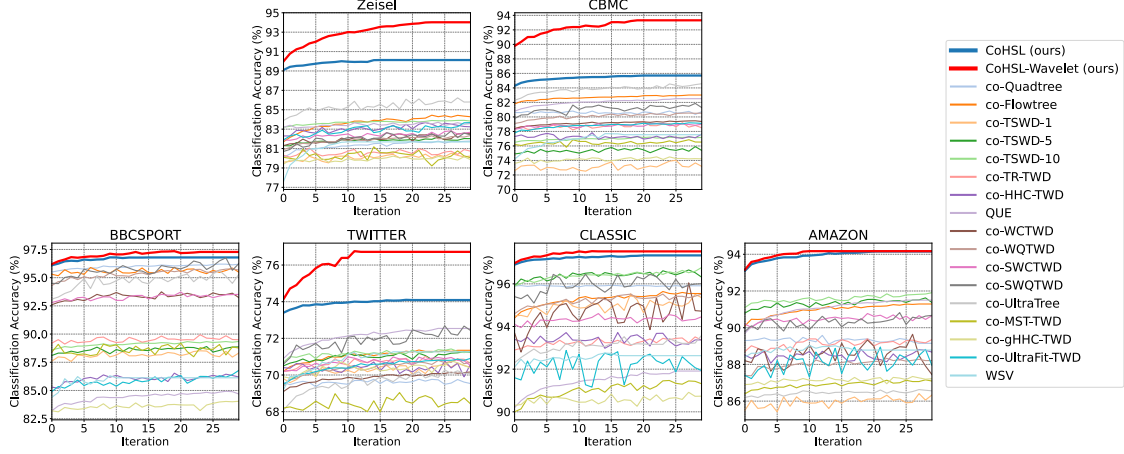


Figure 5: Document and cell classification accuracy over iterations.

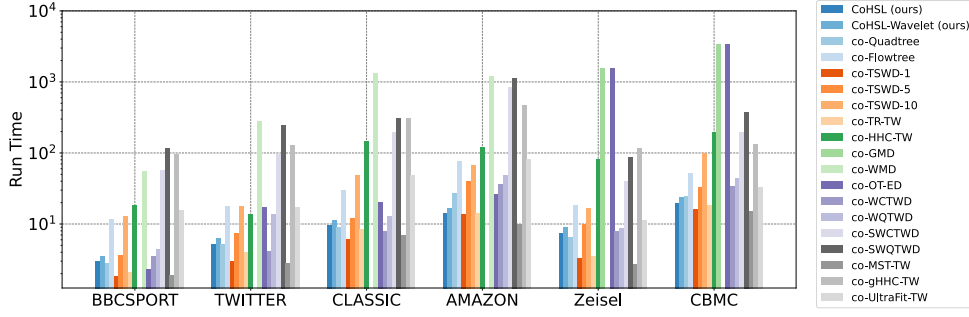


Figure 6: Runtime comparison of CoHSL, CoHSL-Wavelet, competing co-TWDs, and co-OTs on scRNA-seq and word-document datasets.

E.5 CoHSL Using Sinkhorn Divergence

When examining the TWD in the context of underlying hierarchical structures present in rows and columns, the proposed CoHSL in Eq. (6) adopts a regularization function that ensures smoothness across both rows and columns in a data matrix, following the work in Mishne et al. [2019]. Various types of regularization techniques could also be taken into account. For example, the entropic regularization [Cuturi, 2013] approach addresses the OT problem through a matrix scaling algorithm, offering a quadratic time solution. Here, we explore the entropic regularization using the implementation in Flamary et al. [2021] within our CoHSL framework, called Co-Sinkhorn. We apply the Co-Sinkhorn with the embedding distances \mathbf{H}_c and \mathbf{H}_r by

$$\begin{aligned} \mathbf{S}_r(i, i') &= \min_{\Phi_c \in \mathbb{R}^{m \times m}} \langle \Phi_c, \mathbf{H}_c \rangle + \lambda_c \langle \Phi_c, \log \Phi_c \rangle, \\ \mathbf{S}_c(j, j') &= \min_{\Phi_r \in \mathbb{R}^{n \times n}} \langle \Phi_r, \mathbf{H}_r \rangle + \lambda_r \langle \Phi_r, \log \Phi_r \rangle, \end{aligned} \quad \text{s.t.} \quad \begin{cases} \Phi_c \mathbf{1}_n = \mathbf{x}_i, \\ \Phi_c^\top \mathbf{1}_n = \mathbf{x}_{i'}, \end{cases} \quad \text{and} \quad \begin{cases} \Phi_r \mathbf{1}_m = \mathbf{y}_j, \\ \Phi_r^\top \mathbf{1}_m = \mathbf{y}_{j'}, \end{cases}$$

for all $i, i' \in [n]$ and $j, j' \in [m]$, where $\mathbf{y}_j := \mathbf{X}_{\cdot j} / \|\mathbf{X}_{\cdot j}\|_1$ are the normalized features (columns) from the data matrix \mathbf{X} . The entropic regularized OT distances, represented by \mathbf{S}_r for rows and \mathbf{S}_c for columns, are integrated into constructing hyperbolic embedding. This integration aids in reconstructing the embedding distances [Lin et al., 2023] between rows \mathbf{H}_r and columns \mathbf{H}_c , which are then utilized in the subsequent iteration. The regularization parameters λ_r and λ_c are set to be $\{10^{-3}, 10^{-2}, 10^{-1}, 1, 10^1\}$. Fig. 7 presents the comparative classification results for scRNA-seq and word-document datasets using the Co-Sinkhorn with embedding distances. The results demonstrate a significant improvement in performance by the CoHSL and CoHSL-Wavelet over the Co-Sinkhorn, highlighting the effectiveness of our regularization function, which enforces smoothness across both rows and columns, as opposed to entropic regularization in these specific datasets. Further investigation into alternative regularization methods will be considered in our future research.

		CoHSL w/o reg.	CoHSL	QUE	QUE $_{\gamma}$	WSV	WSV $_{\lambda}$	BCOT*	BCOT $_{\lambda}$ *	CCOT*	CCOT-GW*	COOT*	COOT $_{\lambda}$ *
BC	CA	<u>86.2±0.3</u>	87.2±0.4	70.2±0.8	71.9±1.2	68.3±0.4	72.4±3.6	76.9±0.0	84.6±0.0	OOM	OOM	63.1±5.2	61.5±0.0
	NMI	<u>49.7±0.2</u>	51.3±0.3	38.4±0.2	45.3±0.7	31.9±0.9	33.8±2.2	37.2±0.0	48.3±0.0	OOM	OOM	5.4±8.7	5.4±0.0
	ARI	<u>55.4±0.6</u>	57.6±0.7	31.2±1.3	39.8±0.4	34.4±0.8	39.0±0.8	26.7±0.0	46.0±0.0	OOM	OOM	-1.2±2.9	2.2±0.0
LEU	CA	80.3±0.4	81.2±1.1	68.4±0.9	72.3±0.5	66.2±0.4	64.3±4.1	71.2±5.4	80.9±3.8	40.6±0.0	OOM	36.2±2.7	32.5±3.3
	NMI	<u>73.2±0.7</u>	75.4±0.8	54.3±1.2	56.6±0.6	60.8±0.7	61.7±2.3	59.6±6.9	70.9±4.1	0.0±0.0	OOM	14.0±3.6	8.7±2.7
	ARI	<u>56.5±0.3</u>	59.7±1.2	39.4±0.8	42.9±0.4	41.2±0.9	44.8±5.1	39.9±6.3	55.3±3.3	0.0±0.0	OOM	5.4±3.2	-0.5±2.1

Table 6: Clustering performance on gene expression datasets. BCOT, CCOT, CCOT-GW, and COOT are taken from Fettal et al. [2022]. Highest performance in bold and second highest underlined. OOM denotes out-of-memory.

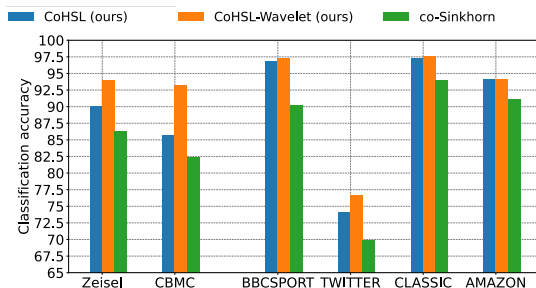


Figure 7: The classification accuracy of CoHSL, CoHSL-Wavelet, and Co-Sinkhorn using embedding distances for scRNA-seq and word-document datasets.

E.6 Co-Clustering on Gene Expression Data

We further evaluate the effectiveness of the coupled TWD matrix from our CoHSL and CoHSL-Wavelet for clustering performance on two gene expression datasets. We test two gene expression datasets in Feltes et al. [2019]: (i) a breast cancer (BC) dataset, which includes gene expression data for 42945 genes across 26 samples divided into two classes, and (ii) a Leukemia (LEU) dataset, consisting of gene expression data for 22283 genes from 64 patients categorized into five classes. We apply Alg. 1 and Alg. 2 to these datasets and apply the k-means clustering [Hartigan and Wong, 1979] to the coupled TWD of the rows and columns from our methods.

We compare our method to six OT-based Co-clustering methods, including (i) applying k-means clustering to QUE [Ankenman, 2014], (ii) applying k-means clustering to WSV [Huizing et al., 2022], (iii) biclustering using OT (BCOT) [Fettal et al., 2022], (iv) Co-clustering through OT (CCOT) [Laclau et al., 2017] and (v) their Gromov-Wasserstein correspondence (CCOT-GW), and (vi) Co-optimal transport (COOT) [Titouan et al., 2020]. Additionally, we assess the impact of regularization on each clustering method, except for CCOT and CCOT-GW, by comparing their performance with and without regularization. In line with the experimental setup in Fettal et al. [2022], we evaluate the clustering performance by the clustering accuracy (CA), normalized mutual information (NMI) [Cai et al., 2008], and adjusted rand index (ARI) [Hubert and Arabie, 1985].

Tab. 6 reports the mean and the standard deviation of the clustering performance averaged over ten runs. The results of BCOT, CCOT, CCOT-GW, and COOT are reported from Fettal et al. [2022]. We see that the CoHSL demonstrates superior clustering performance compared to the competing clustering methods, achieving it with lower standard deviations. Furthermore, we notice that our CoHSL, even without norm regularization, ranks as the second most effective across various evaluation metrics. These results indicate that our CoHSL captures the underlying tree relation of both samples and genes, efficiently incorporating the latent ground hierarchical information in the computation of coupled TWD matrices.